Ceramics International 47 (2021) 31650–31665

Contents lists available at ScienceDirect

Ceramics International

journal homepage: www.elsevier.com/locate/ceramint

Synthesis of 3D nanoflower-like mesoporous $NiCo_2O_4$ N-doped CNTs nanocomposite for solid-state hybrid supercapacitor; efficient material for the positive electrode

Surendra K. Shinde [a], Swapnil S. Karade [b], Nagesh C. Maile [c], Hemraj M. Yadav [a], Gajanan S. Ghodake [a], Ajay D. Jagadale [d], Monali B. Jalak [e], Dae Sung Lee [c], Dae-Young Kim [a,*]

[a] Department of Biological and Environmental Science, College of Life Science and Biotechnology, Dongguk University, Biomedical Campus, 32 Dongguk-ro, Ilsandong-gu, Siksa-dong, 10326, Goyang-si, Gyeonggi-do, South Korea
[b] Electrochemical Energy Laboratory, Department of Chemical and Biomolecular Engineering, Yonsei University, Seoul, Republic of Korea
[c] Department of Environmental Engineering, Kyungpook National University, 80 Daehak-ro, Buk-gu, Daegu, 41566, South Korea
[d] Center for Energy Storage and Conversion, School of Electrical and Electronics Engineering, SASTRA Deemed University, Thanjavur, 613401, Tamilnadu, India
[e] Department of Physics, Shivaji University, Kolhapur, India

ARTICLE INFO

Keywords:
$NiCo_2O_4$
NCNTs
Composite
Deep eutectic solvents
Hydrothermal method
Hybrid supercapacitor

ABSTRACT

In this research work, we report a novel method for developing ternary $NiCo_2O_4$ compounds using deep eutectic solvents (DESs) and a strategy for improving their pseudocapacitive performance. $NiCo_2O_4$ composites with N-doped carbon nanotubes (NCNTs) were fabricated on Ni foam using a hydrothermal method. The electrochemical performance of the $NiCo_2O_4$ was altered with the change in the reaction temperature. The composite of $NiCo_2O_4$ and NCNTs demonstrated a maximum value of specific capacity of 303 mAh g^{-1} at a scan rate of 5 mV s^{-1}. The specific capacity for the composite compound was 1.3-fold greater than that of the pristine $NiCo_2O_4$ sample. For practical applications, we constructed a flexible solid-state hybrid supercapacitor comprised of $NiCo_2O_4$/NCNTs//activated carbon (AC) cells with an excellent energy density of 12.31 Wh kg^{-1}, outstanding power density of 8.96 kW kg^{-1}, and tremendous electrode stability. The three-dimensional mesoporous nanoflowers and nanotubes-like nanostructures of $NiCo_2O_4$ are well-suited for use in hybrid devices as well as convenient for flexible electronic devices.

1. Introduction

Supercapacitors are actively being investigated by researchers for extended commercial use due to the increasing demand for energy storage devices in smart-grid digital electronic gadgets [1]. However, supercapacitors are currently limited by their low energy density compared to Li-ion batteries. Therefore, improving the energy density is the fundamental goal of current supercapacitor research. To this end, many attempts have been made to develop highly efficient supercapacitive materials such as metal oxides, chalcogenides, polymers, polyoxometalates, metal-organic frameworks, Mxene, and siloxene [2,3]. The combination of two different metals to form bimetallic oxides is also an efficient approach to enhance the electrochemical performance of supercapacitors compared to bare metal oxides [1,4].

Recently, various binary and ternary metal oxides have been synthesized for supercapacitor applications including $MnCo_2O_4$, $FeCo_2O_4$, $CoFe_2O_4$, $ZnFe_2O_4$, and $ZnCo_2O_4$, $NiCo_2S_4$, $NiCo_2Se_4$, etc. Among them, the $NiCo_2O_4$ is widely used as a supercapacitor electrode because of its various properties like good electrical conductivity, excellent redox activity, long-term stability, environmental nontoxic, easily available on the earth, and simple preparation [5]. Interestingly, $NiCo_2O_4$ has been utilized for various applications in several research fields such as supercapacitors, Li-ion batteries, water splitting, solar cells, oxygen reduction, hydrogen evolution, and electrocatalysts [1,3]. Recently, many researchers focus on the ternary $NiCo_2O_4$ nanocompounds with various nanostructures for supercapacitor applications. Because, it offers good electrical conductivity and better electrochemical performance, faster redox reaction, multivalence states of Ni^{3+}/Ni^{2+} and Co^{3+}/Co^{2+}, good cycling stability as compared to the binary NiO and Co_3O_4 [3].

* Corresponding author.
E-mail address: sbpkim@dongguk.edu (D.-Y. Kim).

https://doi.org/10.1016/j.ceramint.2021.08.045
Received 8 June 2021; Received in revised form 26 July 2021; Accepted 4 August 2021
Available online 8 August 2021

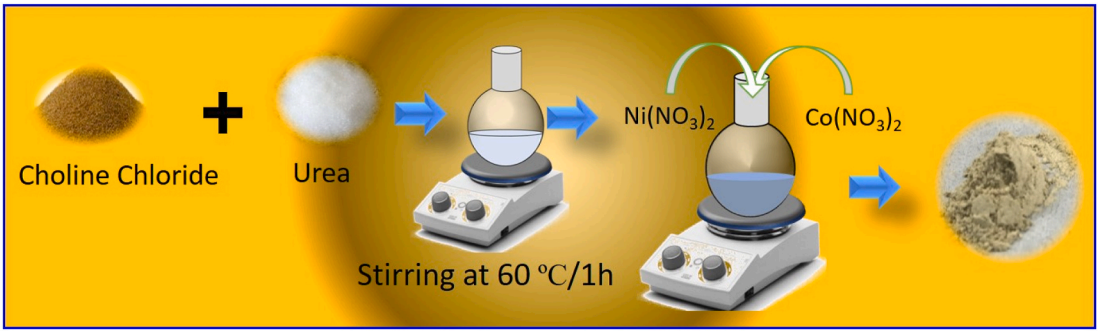

Scheme 1. Schematic presentation of experimental setup of DES method.

There are numerous literature reports on $NiCo_2O_4$ with various structural and morphological modifications for supercapacitor application. Saraf et al. [6] developed porous nanorods like $NiCo_2O_4$ for multifunctional applications that demonstrated significant electrochemical performance with a specific capacity of 163 mAh g^{-1} and 92 % capacity retention. Further, Gu et al. [7] designed 3D nanowires like nanostructures of $NiCo_2O_4$@$NiMoO_4$ nanocomposites for supercapacitor applications that showed the specific capacity of 207 mAh g^{-1} at a current density of 10 mA cm^{-2}. In addition, Kumar et al. [8] prepared the nanoflakes likes Ni/Co oxide-carbon composite thin films using a SILAR method at different carbon contents. This electrode demonstrated a specific capacity of 201 mAh g^{-1} with an excellent cyclic performance of 92 % after 8000 cycles. Xu et al. [9] have synthesized N-doped carbon coated on $NiCo_2O_4$ nanowires array ($NiCo_2O_4$@NC) directly grown on Ni-foam for the supercapacitor application. The $NiCo_2O_4$@NC exhibited an improved specific capacity of 214 mAh g^{-1} which was further utilized as a positive electrode for the fabrication of hybrid supercapacitor. Xu et al. [10] have reported hydrothermal route for the synthesis of $NiCo_2O_4$//AC composite for supercapacitor application. The $NiCo_2O_4$ composite exhibited nanoplates-like morphology with a diameter of 0.5-1 μm which was further coated with AC layer of around 20 nm thickness. The $NiCo_2O_4$//AC composite electrode showed maximum specific capacity of 38 mAh g^{-1} with an excellent cyclic stability of 96 % after 3000 cycles. Many other morphological developments have been reported by Dubal et al. [5], such as nanowire, nanosheet@nanowire core-shell, nanorods, nanoflowers, microspheres, nanoneedles, 2D-nanosheets, nanowire@nanoplate core-shell, nanoparticles, nanotubes, urchin-like, and using different chemical routes. However, to the best of our information, there are no reports on the ternary $NiCo_2O_4$ thin films using DESs with effects of reaction temperatures. After successful formation of the pure ternary $NiCo_2O_4$, we systemically designed a novel experimental setup for compositing the N-doped CNTs and $NiCo_2O_4$ via hydrothermal and DES methods. The optimized $NiCo_2O_4$/NCNTs//AC electrode has been considered for its supercapacitor and hybrid asymmetric devices applications.

In the previous study, we observed that there are no reports on ternary $NiCo_2O_4$ synthesized using the DES method for the supercapacitor applications. Therefore, we planned to synthesize a ternary $NiCo_2O_4$ compound using a cost-effective and simple DES method. The DES method is very effective than other physical and chemical methods because this method is operated very easily and simply, besides, there is no need for special instruments and no loss of chemicals during the experiment, indicating no environmental pollution produced from this method. Also, the DES method provided many advantages comparing to the other physical and chemical methods, including high conductivity, high thermal stability and low viscosity and pressure [11-13]. The DES method offers unique and typical surface morphologies with highly porous nanostructures, these highly porous nanostructures are useful for supercapacitor application because this type of surface morphology provides a higher surface area and easy path to electronic transport.

This manuscript is divided into three parts; the first part describes a strategic development of nanoneedles, nanoflowers, nanoflakes and nanoclusters like surface morphologies of the ternary $NiCo_2O_4$ at different reaction temperatures [14]. The second part depicts the preparation of nitrogen-doped CNTs via the hydrothermal method, and its characterization, furthermore the last and main part focuses on optimization of $NiCo_2O_4$/NCNTs composite electrode for hybrid supercapacitor fabrication. The prepared $NiCo_2O_4$ was analyzed using several measurement techniques to identify its structural, morphological, and surface properties. Electrodes created with the as-prepared $NiCo_2O_4$ were systematically evaluated in 3 M KOH. Finally, we demonstrated the practical feasibility of the $NiCo_2O_4$/NCNTs electrodes by fabricating hybrid supercapacitor devices using AC as a negative electrode. The performance of the hybrid supercapacitor $NiCo_2O_4$/NCNTs//AC device was evaluated using different electrochemical tests.

2. Experimental

2.1. Materials

Analytical grade chemicals such as choline chloride, urea, nickel nitrate hexahydrate $Ni(NO_3)_2.6H_2O$, and cobalt nitrate hexahydrate $Co(NO_3)_2).6H_2O$ were purchased from Sigma Aldrich and used directly without further purification.

2.2. Preparation of deep eutectic solvent (DES)

Choline chloride and urea were added to a flask at a molar ratio of 1:2 and the mixture was constantly stirred at 60 °C. After some time, the entire solid mixture changed to a transparent liquid. The reaction was maintained for 1 h to ensure a stable liquid mixture of choline chloride/urea-based DES. The DES was transferred to an air-tight container and used as a solvent for further reactions.

2.3. Synthesis of $NiCo_2O_4$

2.5 g of $Ni(NO_3)_2.6H_2O$ and 5 g of $Co(NO_3)_2.6H_2O$ were successively dissolved in 20 mL of deionized water (DI). Sequentially, 20 mL of the choline chloride/urea-based DES was slowly added to the above solution with constant stirring at 300 rpm. The four-reaction baths were kept at room temperature (298 K) for 12 h. Finally, a light pink slurry of DES containing $NiCo_2O_4$ was obtained. The solution was filtered using vacuum filtration and the product was rinsed with a large amount of water. The filtered $NiCo_2O_4$ product was dried further at 80 °C in a vacuum oven for 12 h to remove all the DES content in the product. The same reaction procedure was performed at bath temperatures of 323, 348, and 373 K. The synthesized powder was used for the preparation of thin films on Ni foam using the screen-printing method and further analyses were performed. After the assembly of $NiCo_2O_4$ thin films with a homogenous coating, different samples were screen printed on Ni foam. The prepared $NiCo_2O_4$ samples dried naturally and were further annealed at 100 °C for 6 h to evaporate the hydroxide and polyvinyl alcohol (PVA) binder

content. The active mass was constant for the four electrodes; a mass of 0.27 mg cm^{-2} was coated on the Ni foam. Henceforth, the samples will be denoted as NC1, NC2, NC3, and NC4 prepared at 298, 323, 348, and 373 K, respectively. The simplicity of the experimental setup of the DES methods shown in Scheme 1.

2.4. Synthesis of N-doped CNTs using the hydrothermal method

Hollow fixable nanotube-like NCNTs were synthesized using the hydrothermal method. 0.01 g of CNTs were dispersed in 100 mL of DI water with continuous stirring. The solution was kept under ultra-sonication using a probe sonicator for 45 min at 75 Hz. To the above solution, 1 g of urea and 16 mL of ammonia solution were added drop-wise. The solution was placed in a 250 mL Teflon-lined autoclave and kept at 180 °C for 6 h to achieve the deposition of NCNTs on the Ni foam [15,16]. Then, the autoclave was cooled naturally to room temperature and the NCNTs-coated Ni foam was cleaned several times with double distilled water to remove loosely deposited particles. Afterward, the NCNTs-coated Ni foam was used to create a composite with the optimized as-prepared NC2 for further analysis.

2.5. Synthesis of $NiCo_2O_4$ and NCNTs composite thin films using screen printing method

To prepare NC2/NCNTs composite thin films, we used the NCNTs-coated Ni foam as a base and created a composite with the optimized NC2 samples using screen printing [17]. Further details of the screen-printing method and final preparation of the sample are given in section 2.3. This synthesized composite was designated as NC2/NCNTs and used for further structural, morphological, and electrochemical studies.

2.6. Characterization

The structures of the as-prepared and composite nanomaterials were confirmed using powder X-ray diffraction (XRD, Bruker D8 Advanced). Raman spectroscopy (Jobin-Yvon LabRam-HR) and Fourier-transform infrared spectroscopy (FT-IR, Nicolet 6700) were used to examine the relationships between the vibrational modes and chemical composition, respectively. X-ray photoelectron spectroscopy (XPS) was used to determine the chemical composition and elemental information (ULVAC-PHI Quantera SXM). The surface morphology of the as-

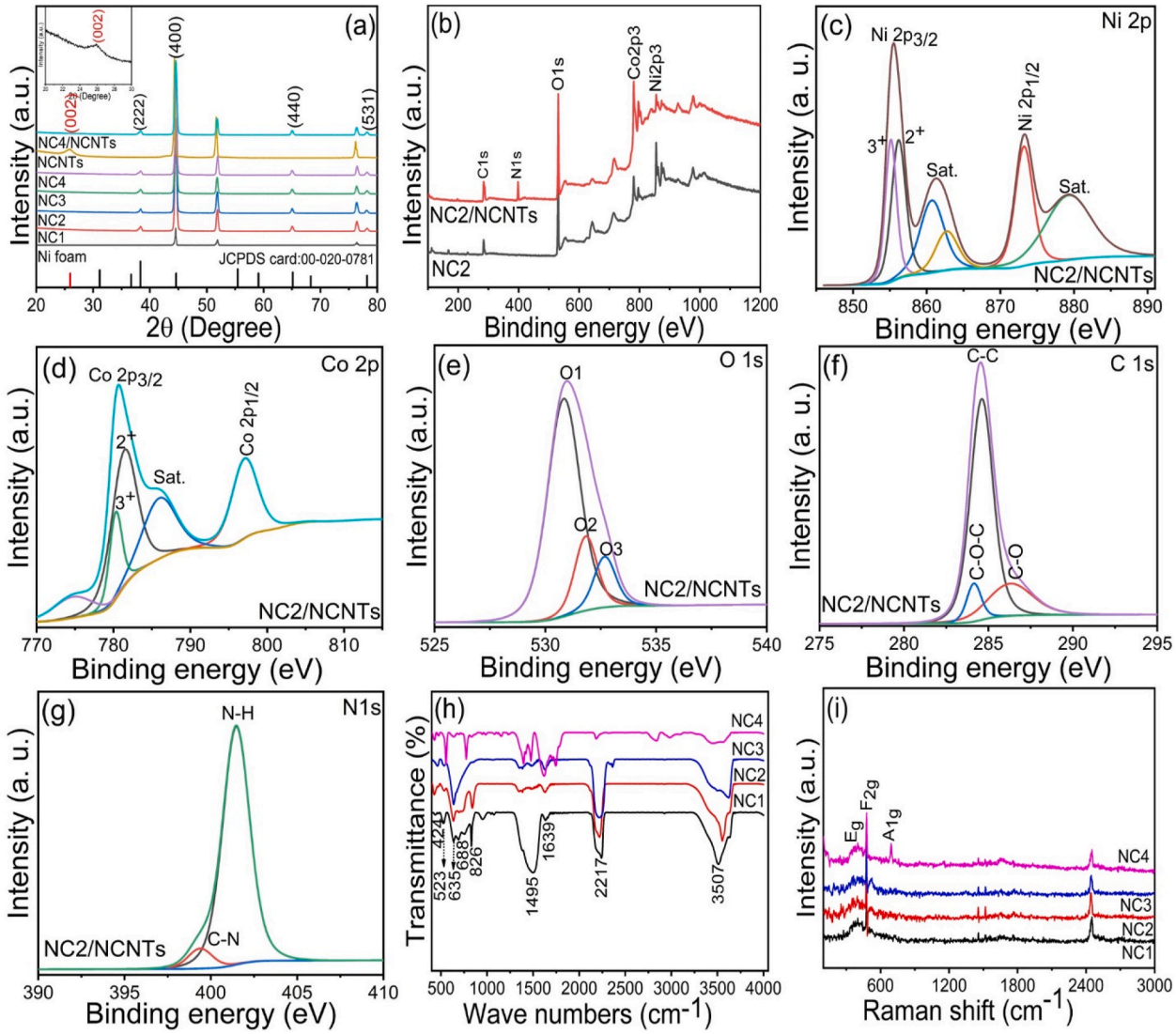

Fig. 1. (a) XRD patterns of NC1, NC2, NC3, NC4, NCNTs, and composite of NC2/NCNTs samples, (b) XPS survey scan spectrum of optimized NC2 and composite of NC2/NCNTs samples, (c-g) Core level of Ni 2p, Co 2p, O1s, C1s, and N1s of NC2/NCNTs sample, respectively, (h) FT-IR spectra of the NC1, NC2, NC3, and NC4 samples, and (i) Raman spectra of the NC1, NC2, NC3, and NC4 samples.

prepared and composite samples was studied using field emission scanning electron microscopy (FE-SEM; JEOL JSM-7100) and high-resolution transmission electron microscopy (HR-TEM; JEOL JEM-2100). The supercapacitor properties were investigated using a three-electrode system with the as-prepared and composite electrodes, Pt, and Ag/AgCl as the working, counter, and reference electrodes, respectively. Electrochemical analyses consisting of cyclic voltammetry (CV), galvanostatic charge-discharge (GCD), and electrochemical impedance spectroscopy (EIS) were carried out on a Versa STAT 3 machine in 3 M KOH. The electrochemical tests for CV and GCD were performed at scan rates and current densities of 5-100 mV s^{-1} and 10-30 mA cm^{-2}, respectively. The EIS studies were performed within the frequency range of 0.1-100 kHz [18].

2.7. Fabrication of flexible solid-state hybrid (SSHSc) supercapacitors

2.7.1. Preparation of PVA-KOH solid gel-like electrolyte

Firstly, we dissolved 2 g PVA in 25 mL double distilled water with continuous stirring at 60 °C for 2 h. Afterward, 2 g KOH was dissolved in 10 mL double distilled water and added dropwise to the PVA solution with a 5 min interval between drops under continuous stirring. After 12 h, the PVA and KOH solution was fully transformed into a whitish transparent gel [18].

2.7.2. Assembly of SSHSc

Two-electrode flexible hybrid supercapacitor pouch cells were fabricated with the $NiCO_2O_4$/NCNTs composite as the positive electrode and commercial AC as the negative electrode. The prepared PVA/KOH gel and printing paper were used as a solid-state electrolyte and separator, respectively. The CV, GCD, and EIS were performed using the same workstation and the electrochemical parameters were calculated [18]. The specific capacity (C_s) of the $NiCo_2O_4$ electrodes was calculated with the formulae below for the CV curves and charge-discharge curves [18];

$$C_s(mAhg^{-1}) = \frac{\int I(V)dV}{mv \times 3.6} \quad [1]$$

$$C_s(cg^{-1}) = \frac{\int I(V)dV}{mv} \quad [2]$$

$$C_s\left(mAhg^{-1}\right) = \frac{I\int Vdt}{mV \times 3.6} \quad [3]$$

The specific energy and power were calculated using the following equations [18].

$$C\ (Fg^{-1}) = \frac{I\int Vdt}{mV^2} \quad [4]$$

$$\text{Specific Energy (SE) (Wh kg}^{-1}) = \frac{1}{2 \times 3.6} CV^2 \quad [5]$$

$$\text{Specific Power (SP) (W kg}^{-1}) = \frac{\text{SE} \times 3600}{T_d} \quad [6]$$

3. Results and discussion

3.1. Reaction mechanism

The reaction kinetics for the synthesis of $NiCo_2O_4$ were determined with the following steps. The heated DES mixture released ammonia from urea as depicted in the following reaction.

$$CO(NH_2)_2 \rightarrow NH_3 + HCNO \quad [7]$$

Further, the added $Ni(NO_3)_2$ and $Co(NH_3)_2$ directly reacted with the ammonia due to the anhydrous DES solution, leading to the formation of Ni and Co ammonium nitrate.

$$Ni(NO_3)_2 + NH_3 \rightarrow Ni(NH_3)(NO_3)_2 \quad [8]$$

$$Co(NO_3)_2 + NH_3 \rightarrow Co(NH_3)(NO_3)_2\uparrow \quad [9]$$

The addition of water helped create a suitable reaction environment for the Ni and Co ammonium nitrate to form $NiCo_2O_4$ as depicted in the reaction below:

$$Ni(NH_3)(NO_3)_2 + 2Co(NH_3)(NO_3)_2 + 4H_2O \rightarrow NiCo_2O_4 + 6HNO_3 + 3NH_3 + H_2\uparrow \quad [10]$$

During the reaction, the $NiCo_2O_4$ nanoparticles aggregated in the form of nanoneedles, nanoflowers, nanoflakes, and clustered nanoflakes at different reaction temperatures.

3.2. X-ray diffraction (XRD) study

XRD was used to confirm the crystal structure, phase, and effect of the reaction temperature on the structural properties. Fig. 1(a) presents the XRD patterns of the $NiCo_2O_4$ samples prepared at various temperatures using DES and the optimized NCNTs sample composite with NC2 on Ni foam (NC2/NCNTs). All $NiCo_2O_4$ samples were well-matched to the standard JCPDS card number (00-020-0781), indicating the formation of a cubic crystal structure. All XRD patterns showed the prepared $NiCo_2O_4$ samples were in a highly pure phase and no other binary phase or impurities were identified. As the preparation temperature was increased to 298 K, additional diffraction peaks appeared on the main diffraction peaks for the stable ternary phase of $NiCo_2O_4$. From the XRD results, four major peaks were observed at 2θ of 38.32, 44.52, 64.05, and 78.11°, related to the (222), (400), (440), and (531) crystalline planes, respectively. All of the above peaks were in agreement with the JCPDS card, indicating a pure ternary $NiCo_2O_4$ phase was formed in all samples [19]. The NCNTs show the XRD patterns for the NCNTs developed with the hydrothermal method. The comparison of the NC1-NC4, NCNTs, and NC2/NCNTs composite shows the both materials are presented in good order. The diffraction peaks at 38.32, 44.52, 64.05, and 78.11°, corresponded to the $NiCo_2O_4$ phase and the peaks at 25.91° were related to the NCNTs. This indicates that both $NiCo_2O_4$ and N-doped CNTs were present in the prepared composite. These results were in good agreement with the previously reported work [20,21].

3.3. X-ray photoelectron spectroscopy study

XPS analysis was performed for a detailed assessment of the electronic valence and chemical state of the optimized NC2 and composite NC2/NCNTs samples. Fig. 1(b) shows the survey spectra for NC2 and NC2/NCNTs samples [22]. Peaks correspond to Ni, Co, and O appeared in the spectrum of NC2, and peaks related to Ni, Co, O, C, and N appeared in the spectrum of the NC2/NCNTs composite, as expected. The core levels of Ni 2p, Co 2p O1s, C1s, and N 1s are presented in Fig. 1 (c-g). At the Ni 2p core level, two main peaks observed at the binding energies of 855.45 and 873.34 eV were attributed to Ni $2p_{3/2}$ and Ni $2p_{1/2}$, respectively, corresponding to the Ni^{2+} species [23]. Two more peaks were positioned at 861.26 and 879.85 eV, which were related to the satellite peaks of the Ni 2p species (As shown in Fig. 1(c)), [24]. The peak at 780.63 and 797.210 eV corresponded to Co $2p_{3/2}$ and Co $2p_{1/2}$, while the peak at 786.32 eV was ascribed to the satellite peak for the Co^{2+} species, as shown in Fig. 1(d) [25]. Fig. 1(e) shows the core level of the O 1s spectrum for the composite NC2/NCNTs material. The core level shows the three main peaks at 530.85, 531.81, and 532.69 eV, which correspond to the typical metal−O_2 and the water defect sites in O_2, respectively, confirming the presence of rich defect sites on the surface of the NC2/NCNTs [24-28]. Upon closer observation of Fig. 1(e), the main peak for the O1s at the binding energy of 531.81 eV was ascribed to the metal−oxygen bonds in the NC2/NCNTs [25-28]. Fig. 1

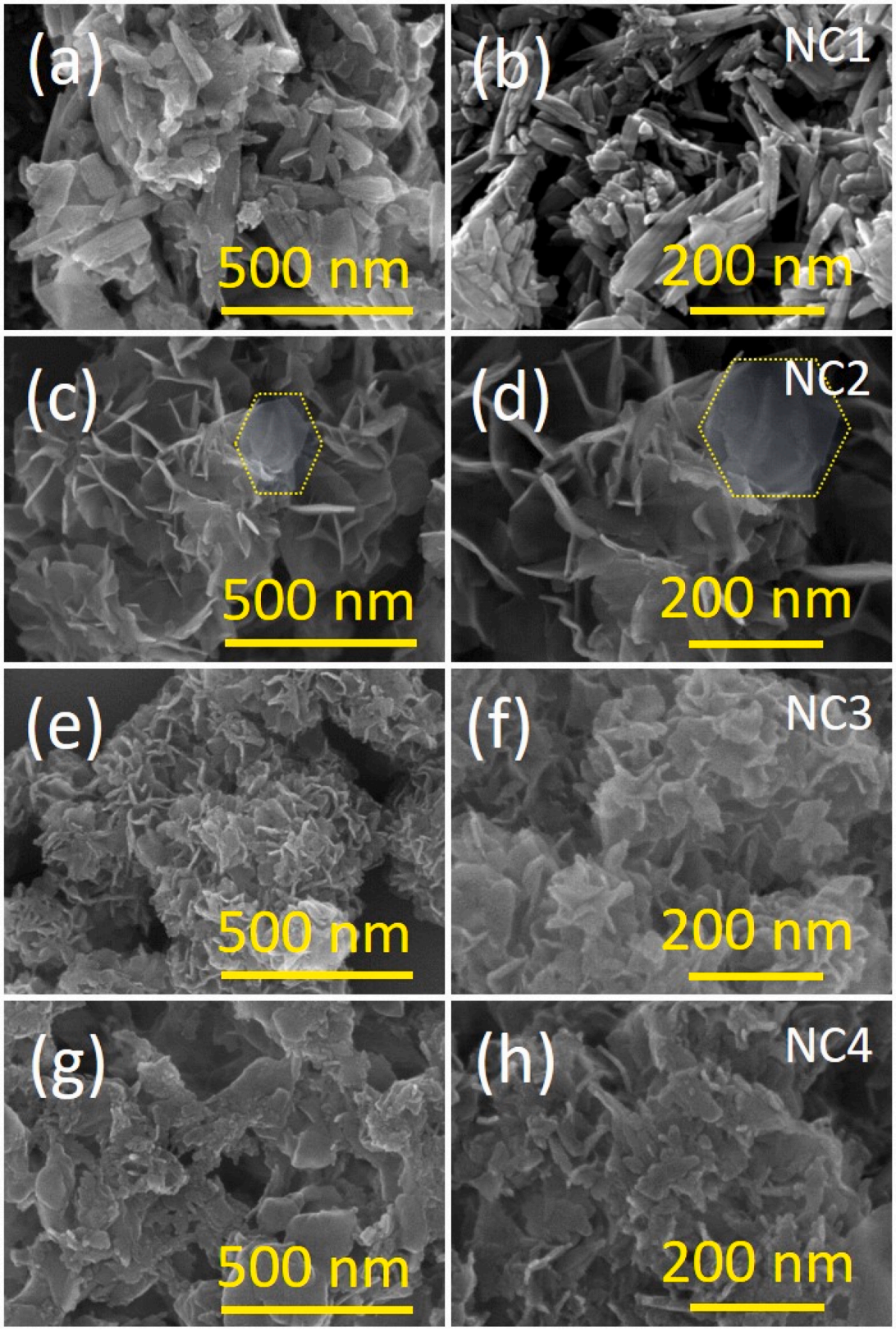

Fig. 2. (a-h) FE-SEM of as-prepared NC1, NC2, NC3, and NC4 samples with different magnifications, respectively.

(f) and (g) presents the core level of the C1s and N1s spectrum for the NC2/NCNTs, respectively. The peaks located at the binding energies of 284.13, 284.55, and 286.39 eV correspond to the C-O-C, C-C, and C-O bonds, respectively [28,29]. The N1s core level shows that nitrogen was effectively doped in the final NC2/NCNTs product. The peaks located at 399.27 and 401.44 eV are related to the pyridinic/pyrrolic, and graphitic state of nitrogen [28,30]. The XPS survey and core-level spectrum show that the Ni, Co, O, C and N elements were present,

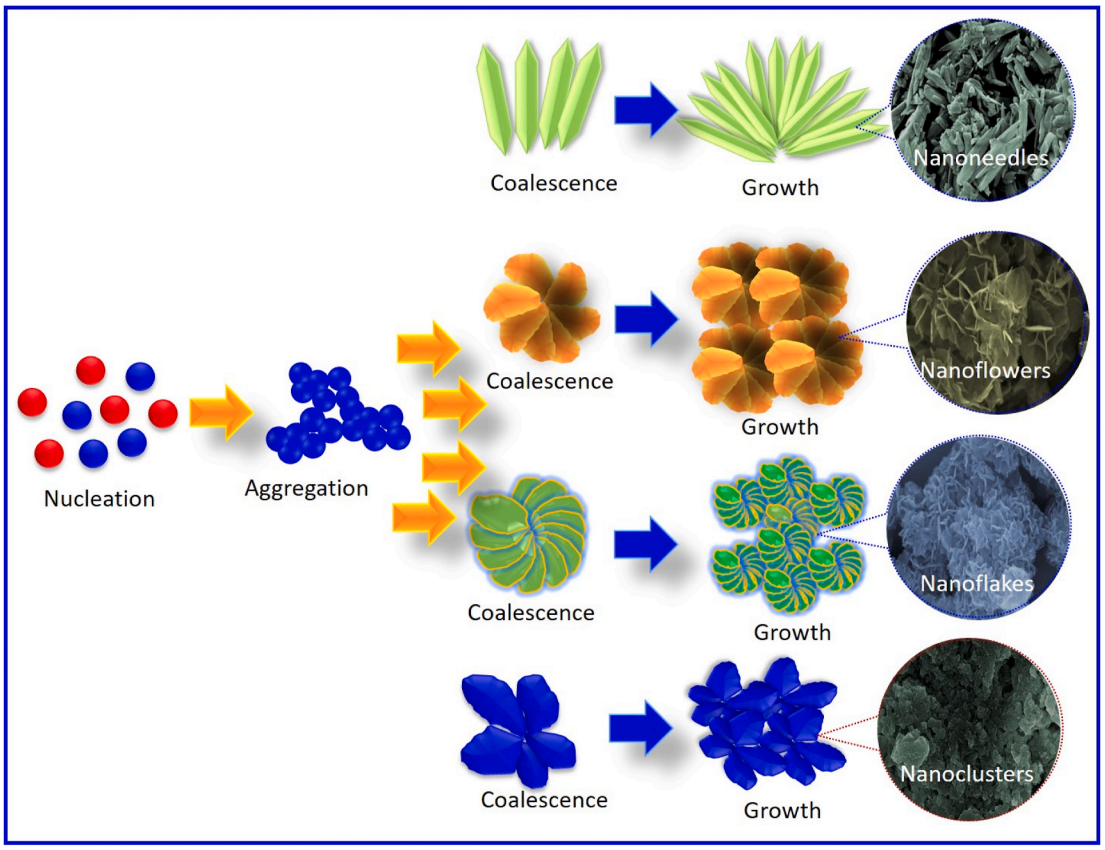

Scheme 2. Growth mechanism of $NiCo_2O_4$ thin films prepared from DES method.

suggesting that the synthesized sample is pure, which was also confirmed by EDS analysis.

3.4. FT-IR and Raman spectroscopy study

FT-IR analysis was used to study the effect of the reaction temperatures on the functional group and stretching vibrational modes of $NiCo_2O_4$. Fig. 1(h) presents the FT-IR spectrum of the $NiCo_2O_4$ nanomaterial prepared at different reaction temperatures. The main sharp peaks located at 523-688 cm^{-1} were assigned to the octahedral site for the Co-O and Ni-O stretching vibrational modes and demonstrated the vibrational bands of Ni and Co oxide appeared in all samples of $NiCo_2O_4$ [19,31]. Four other peaks were located at 1495, 1639, 2217, and 3507 cm^{-1}, corresponding to the stretching vibration modes of the C═C, CH_2, and O-H groups. At a temperature of 373 K, the peaks located at 2217 and 3507 cm^{-1}, showing that the peak intensity decreased. From the FT-IR studies, we observed that the peak absorption intensity changed depending on the bath temperature as well as the surface morphology and functional groups present in the prepared samples [32]. Fig. 1(i) presents the Raman spectrum for $NiCo_2O_4$ prepared at different reaction temperatures in the range of 0-3000 cm^{-1}. In the Raman spectrum, three main absorption peaks were observed at 438.45, 474.52, and 693.34 cm^{-1} related to the three different modes E_g, F_{2g}, and A_{1g} [33]. These E_g, F_{2g}, and A_{1g} modes corresponded to the $NiCo_2O_4$ vibrational modes, indicating that the prepared $NiCo_2O_4$ was highly pure. Two more absorption peaks were located at 1461.62 and 1520 cm^{-1}, corresponding to the D and G absorption bands of graphene [34-37].

3.5. Surface morphology study

FE-SEM was used to study the surface morphologies of the as-prepared $NiCo_2O_4$ with different reaction temperatures. Fig. 2(a-h) presents the FE-SEM images of the $NiCo_2O_4$ samples with different magnifications. From the FE-SEM results, we observed that the surface morphology of $NiCo_2O_4$ samples alters from nanoneedles to nanoclusters of the nanoflakes as the reaction temperature increased. The surface morphology of the $NiCo_2O_4$ sample prepared at room temperature (298 K) shows the horizontal growth of the nanoneedles-like surface formed with an individual length 300-350 nm and a thickness of 20-30 nm (as shown in Fig. 2 (a, b)). At high magnification (Fig. 2 (b)), the FE-SEM image showed that all the conical nanoneedles were deposited in a horizontal direction on the surface of the $NiCo_2O_4$ sample [37,38]. As the reaction temperature increased to 323 K, the surface morphology is developed from nanoneedles to the typical flower-like surface morphology of the $NiCo_2O_4$ sample. At high magnification (Fig. 2(d)), the FE-SEM image clearly shows alteration in the growth direction from horizontally deposited nanoneedles to the vertical growth of the nanoflakes like the $NiCo_2O_4$ sample. It may be due to the reduction of the surface energy with increasing reaction temperature from 298 to 323 K. The thickness and length of the uniform and interconnected nanoflakes are 100-120 and 10-20 nm as clearly seen in Fig. 2(d). The marked area shows the individual hexagonal nanoflakes are highly porous. This type of surface morphology provides higher porosity and specific surface area [37,38], which are more beneficial for energy storage applications because the porous surface area is useful for the ion/electron transformation during electrochemical testing [35-38]. Further, with increased reaction temperature to 348 K, the nanoflowers were converted into interconnected nanoflakes-like surface morphology, which may be the nucleation rate higher than the growth rate (Fig. 2 (e, f)) [14]. FE-SEM results of the NC3 samples clearly show that the surface of morphology was fully covered with highly compact, aggregated, and interconnected nanoflakes-like chains of nanoflowers [36]. The diameters of typical nanoflowers were around 400-500 nm, with an individual thickness of nanoflakes 15-20 nm and a chain length of around

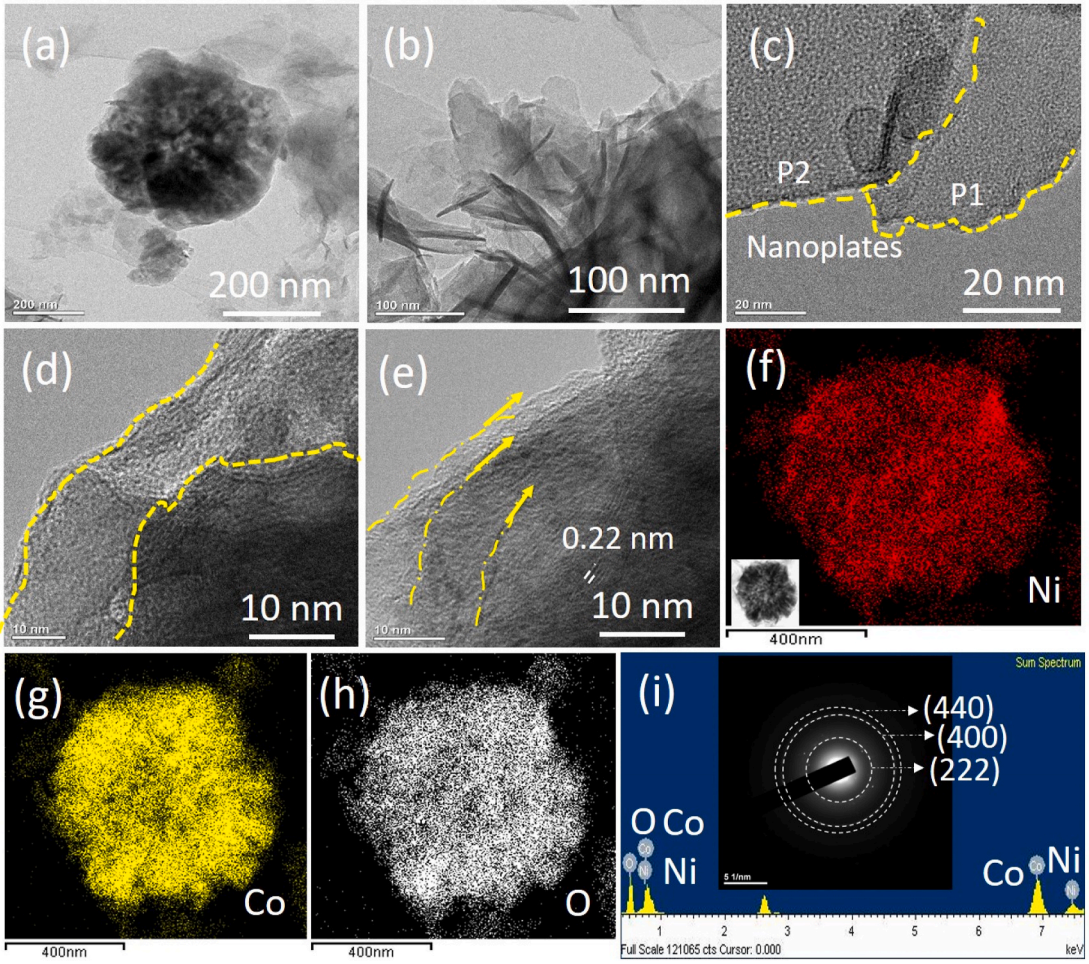

Fig. 3. (a-e) TEM images, (f-h) elemental mapping, and (i) EDS of optimized NC2 sample, inset shows the SEAD patterns of NC2 sample.

1-1.5 μm. Compact nanostructures are poorly suitable for supercapacitor applications because they provided slower ion/electron transformation during electrochemical testing [35-37]. To obtain more detailed information about the surface morphology and confirm the effect of the higher temperature on the surface morphology, we further increased the temperature to 373 K. The significant changes were observed in the surface morphology at a higher temperature (Fig. 2 (g, h)). The FE-SEM results clearly show the overgrowth formed on the surface of the $NiCo_2O_4$ sample, because of the fast rate of nucleation and low development of the growth, and which indicates the reduction of the surface energy of the material [36-38].

We have presented a possible growth formation mechanism for different nanostructures as shown in Scheme 2. The preparation of nanomaterial depends on the development of a solid phase from the supersaturated solution of the Ni, and Co ions. In this procedure, four main steps are involved such as aggregation, nucleation, coalescence and growth of nanomaterials. In the first step, a heterogeneous reaction formed and bunches of the nanomaterials are formed and in the second step the aggregation of the particles formed on the center of nucleation of the nanomaterials. The third and last steps are related to the coalescence and growth of nanostructure, respectively. In the coalescence process, nanoparticles are aggregated to each other and started the formation of the nanostructures. Finally, in the fourth step, the growth of nanostructures developed on the surface of nanomaterials. This growth of nanomaterials depends on the ion-by-ion mechanism, which is related to the ion-by-ion formation of the nanostructure on the surfaces of the nanomaterials [14]. Fig. 2 and Scheme 2 indicate the deposition temperature is useful for the development of the different surface morphology.

TEM, elemental mapping, EDS, and SAED were used to obtain more information on the surface morphology, composition, and elemental mapping of the optimized NC2 samples. Fig. 3(a-e) presents the TEM images of the NC2 sample, which indicates the interconnected chain of numerous flowers over the surface of the carbon grids (shown in Fig. 3 (a)) [33,38]. At a higher magnification, the top view of a rose flower-like surface is noticeable (shown in Fig. 3(b)). The TEM results clearly shows the number of interconnected highly mesoporous nanoplates that grow in the vertical direction with a regular shape and an average length and thickness of 100-150 nm and 5-10 nm, respectively. The lower thickness and highly porous nanoplates are more useful for supercapacitor application, because this type of surface morphology provides a large electroactive area, making easy contact between the electrolyte and electrode interface [33]. The elemental mapping of the optimized NC2 sample shows the uniform distribution of the Ni, Co and O elements, which indicates the formation of the pure ternary $NiCo_2O_4$ nanocompounds (Fig. 3(f-h)). The inset of Fig. 3(i) presents SAED pattern of the optimized NC2 and clearly shows the three major rings. In the SAED pattern, the lattice planes are indexed to (222), (400), and (440), which confirm the polycrystalline nature of the nanoplates-like $NiCo_2O_4$ [39-43]. EDS was used to confirm the chemical composition of the optimized NC2 sample and presented in Fig. 3(i). The EDS results confirm the presence of Ni, Co, and O in the optimized NC2 sample with atomic weight percentages of about 29.5, 27.81, and 42.69, respectively. The TEM, mapping, and EDS results indicate the formation of a highly pure phase of $NiCo_2O_4$ [20].

We developed a new technique to improve the electrical properties of

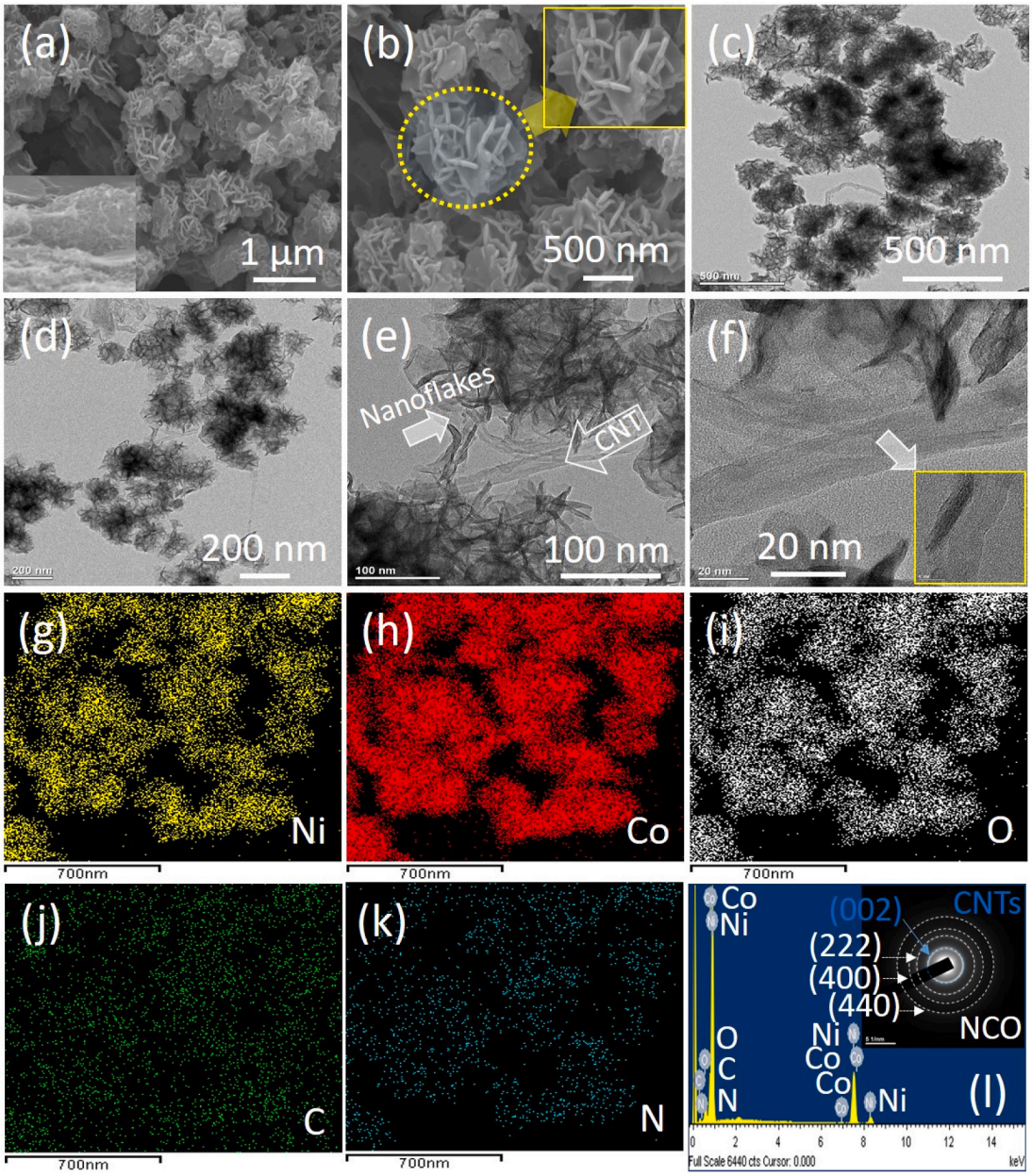

Fig. 4. (a, b) FE-SEM images, inset shows the cross section of the NC2/NCNTs sample, (c-f) TEM images of the NC2/NCNTs sample, (g-k) elemental mapping of the Ni, Co, O, C and N elements, and (l) EDS of optimized composite NC2/NCNTs sample, inset shows the SEAD patterns of NC2/NCNTs sample.

the $NiCo_2O_4$ electrodes. NCNTs samples were prepared using the hydrothermal method and composites with the optimized NC2 sample. FE-SEM was used to observe the surface morphologies of the as-prepared NCNTs and composite of the NC2/NCNTs with different magnification. The FE-SEM images for the composite materials are shown in Fig. 4 (a and b), respectively. To understand the construction of the composite, we evaluated the cross-sections of the composite samples (Fig. 4(a)) and observed the nanoflakes layer of $NiCo_2O_4$ deposited on the nanotubes of the NCNTs. The cross-section views of the composites showed that the nanotubes layers and nanoflakes were interconnected and distributed across each other. The FE-SEM represented the formation of the uniform formation of the nanoflower-like surface morphology on the surface of the composite materials with the individual length and thickness of the nanosheet of 500-600 nm and a 50-60 nm [44,45]. The TEM images of NC2/NCNTs composite displays both nanoflowers- and nanotube-like nanostructures are observed, indicating that both compounds were well ordered deposited on the Ni foam (shown in Fig. 4(c-f)). At higher magnification of the TEM images (Fig. 4(e)), we observed that the mesoporous nanoflakes were fully grown on the nanotubes. This type of hybrid surface morphology is suitable for improving electrochemical performance because it provides an easy and faster path for ion-electron transformation from the surface of electrode and electrolyte [46,47]. The homogeneous distribution and formation of Ni, Co, O, C and N elements are observed in the elemental mapping (Fig. 4(g-k)). SAED patterns also provide information on the crystal structure (inset of Fig. 4 (l)). The SAED patterns depicted four diffraction rings, out of these (222), (400), and (440) planes correspond to $NiCo_2O_4$ nanomaterial and one diffraction ring indexed to (002) plane attributes to the N-doped CNTs, which confirmed the polycrystalline nature with a hybrid phase of the $NiCo_2O_4$ and N-doped CNTs material. The SAED patterns matched in good order to the XRD and XPS results. Fig. 4(l) shows the EDS of NC2/NCNTs composite, shown the presence of Ni, Co, O, N and C elements, which indicates the formation of the NC2/NCNTs composite. The EDS of the NC2/NCNTs showed atomic percentage of Ni, Co, O, N and C

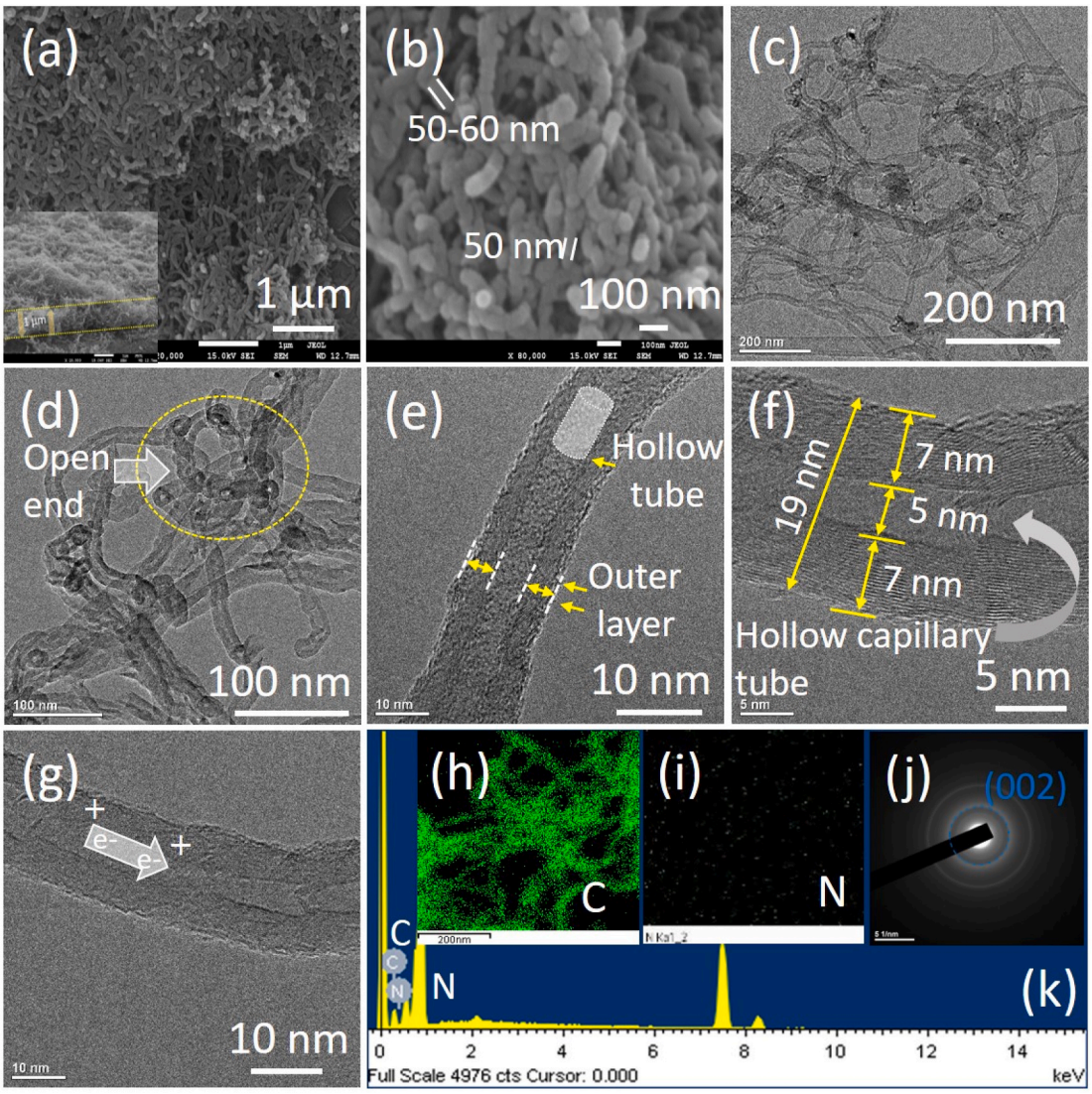

Fig. 5. (a, b) FE-SEM images with different magnification, inset shows the cross section, (c-g) TEM images with different magnifications, (h, i) elemental mapping of C and N elements, (j) SEAD patterns and (k) EDS of the NCNTs samples.

for about 24.45, 21.65, 19.82, 25.69, and 8.46% on the samples. The EDS and elemental mapping analysis confirmed the formation of both $NiCo_2O_4$ and N-doped CNT compounds in the NC2/NCNTs composite.

Fig. 5(a-k) shows the FE-SEM, TEM, elemental mapping and EDS images of NCNTs thin films prepared on Ni foam using the hydrothermal method. The FE-SEM results clearly show that all surfaces of the Ni foam were uniformly covered in nanotube-like nanostructures with diameters of around 50-60 nm (as shown in Fig. 5 (a, b)) [48,49]. At higher magnifications, FE-SEM images shows the all nanotubes are interconnected with each other and both ends of the nanotube are open, which is more suitable for the supercapacitor applications because tube-like nanostructures provided higher active surface area, faster transformation of ions, fast faradaic reactions. Fig. 5(c-g) shows the TEM images of the NCNTs with different magnification. The lower magnification TEM images show the nanotubes were more flexible and open-ended with a porous nanostructure (Fig. 5 (c, d)). However, at higher magnification, we observed that both ends of the nanotubes were open and the nanotubes were distributed in two regions: the outer layer and the inner hollow cylindrical layer (as shown in Fig. 5(e-g)). The thickness of the outer layer was very low, and the inner diameters of the cylindrical nanotubes were 19 nm and 7 nm, respectively. The elemental mapping of the N-doped CNTs samples shows the uniform distribution of C and N elements on the surface of nanotubes (Fig. 5 (h, i)), which indicates the presence of C and N elements in NCNTs sample. The SAED patterns of the NCNTs shows the diffraction ring of the (002) plane, which is related to the carbon nanotube (Fig. 5 (j)). Fig. 5 (k) presents the EDS results of the N-doped NCNTs samples. EDS results showed uniform distributions with atomic percentage of carbon and nitrogen of 98% and 2%, respectively. The EDS and elemental mapping results are well matched.

3.6. BET analysis

The specific surface area, pore size distributions, and pore volume are important parameters to improve the electrochemical performance of $NiCo_2O_4$. Fig. 6(a-d) represents the N_2 adsorption/desorption isotherm of NC1, NC2, NC3 and NC4 samples prepared at different reaction temperatures, respectively. All BET curves of $NiCo_2O_4$ samples show the type 4 adsorption/desorption isotherm with H3 hysteresis loops, which could be related to the mesoporous nanoflakes like $NiCo_2O_4$ nanoflowers. The pore size distributions of NC1, NC2, NC3 and NC4 samples are shown in the inset of Fig. 6(a-d). All pore size distributions curves show the pore size ranges from 2 to 5 nm, suggesting the mesoporous nature of all prepared samples. These results indicate

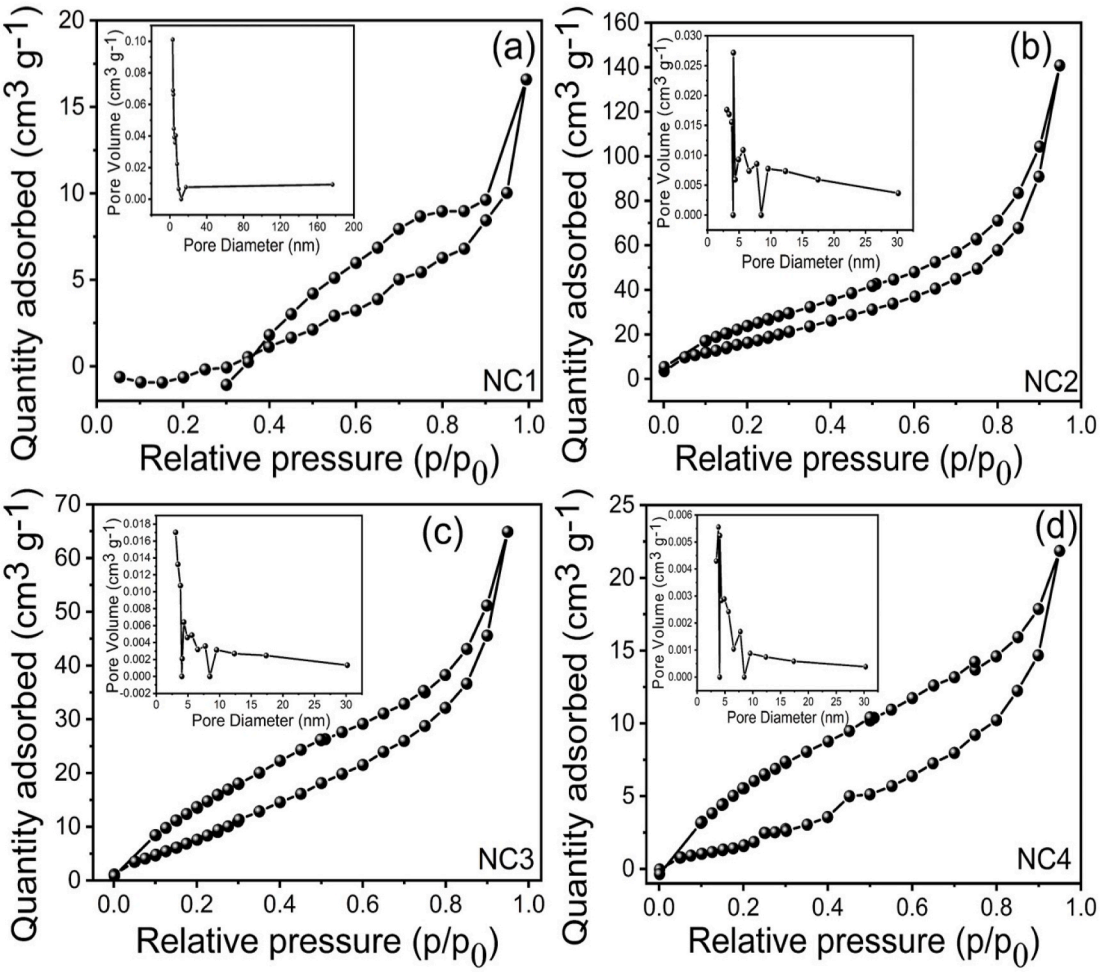

Fig. 6. (a-d) BET results of NC1, NC2, NC3, and NC4 samples, insets shows the pore size distributions of samples.

different pore volumes with the same pore diameter and mesoporous, which may be due to the different surface morphology. The BET surface areas for nanoneedles, nanoflowers, nanoflakes and nanoclusters are 22.66, 82.33, 43.46, and 16.60 $m^2\ g^{-1}$, respectively. These results indicate of NC2 provided a higher specific surface area compared to the other $NiCo_2O_4$ samples, because highly porous and vertically grown nanoflakes provided a more specific surface area. These types of nanostructures and lower pore diameter of samples are more useful for the supercapacitor application because it provides higher specific surface area and easy path for ion transformation. Moreover, BET results indicate the surface area of NC3 and NC4 samples decreases with increased reaction temperature, which is the main reason for the decrease in the electrochemical performance of $NiCo_2O_4$ electrodes. Previously, similar reports are available [14]. This BET analysis strongly supports to the surface morphologically analysis.

3.7. Electrochemical study

The electrochemical properties of the $NiCo_2O_4$ electrodes synthesized at different reaction temperatures were analyzed in a three-electrode system with a potential window of 0.0-0.5 V using 3 M KOH. Figs. 7(a) and S1 (a-c) present the CV curves for the $NiCo_2O_4$ electrodes at different scan rates from 5 to 100 mV s^{-1} within a potential window of 0.0-0.5 V. The CV curves for the NC1, NC2, NC3, and NC4 electrodes show current densities of 63.86, 94.29, 73.61, and 28.19 mA cm^{-2} within a unit area at a scan rate of 100 mV s^{-1}. Therefore, the NC2 electrode had the highest current density compared to the other three electrodes, possibly because the nanoflakes-like nanostructure provided a larger specific surface area [50]. The CV curves clearly showed strong redox peaks at 0.13 and 0.33 V potential values due to reversible Faradaic redox reactions [51,52]. Moreover, we observed that the reaction temperature affected the nature of the CV curves. Reaction temperatures of 298 and 323 K were quite similar, with only a difference in the current. We observed similar results for the surface morphology. During the electrochemical test, the following reaction occurred between the $NiCo_2O_4$ electrodes and KOH electrolytes, in accordance with the Faradaic reactions [51].

$$NiCo_2O_4 + H_2O + OH^- \leftrightarrow NiOOH + 2CoOOH + e^- \quad [11]$$

$$CoOOH + OH^- \leftrightarrow CoO_2 + H_2O + e^- \quad [12]$$

Furthermore, the current density increased as the scan rates increased, and the peak position of oxidation was higher (0.30-0.35 V) and the reduction peak shifted to the lower potential window (0.17-0.13 V). Fig. S1(d) shows the specific capacity of the NC1, NC2, NC3, and NC4 electrodes with different scan rates. The specific capacity values for the NC1, NC2, NC3, and NC4 electrodes were 119, 237, 189, and 101 mAh g^{-1}, respectively, which indicates NC2 electrode showing the highest specific capacity. The mesoporous interconnected nanoflakes-like surface provides a more specific surface area and the lower pore diameter of the vertically grown hexagonal nanoflakes structure leads to its highest specific capacity. The other $NiCo_2O_4$ samples shows specific capacity values reduced as compared to NC2 samples attributed to low specific surface area and pore diameters, which may be due to compact nanostructures. These compact like surface is not suitable for the ion exchange or ion transfer during the electrochemical process. These BET

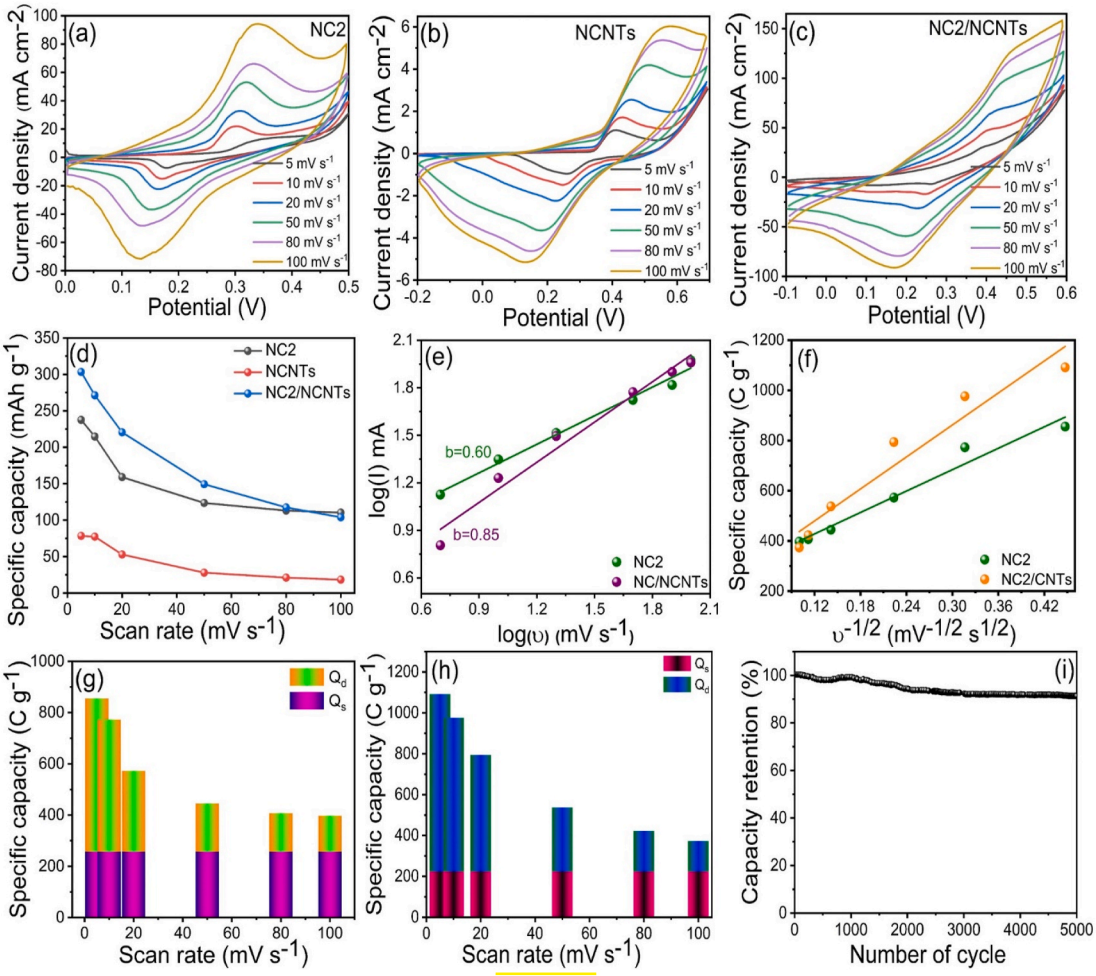

Fig. 7. (a-c) CV measurements of NC2, NCNTs, and NC2/NCNTs composite, respectively, (d) specific capacity of NC2, NCNTs, and NC2/NCNTs composite with different scan rates, (e) log of peak current as a function of the log of scan rate, (f) total charge QUOTE as a function of reciprocal square root of scan rate, contribution from QUOTE and QUOTE to the QUOTE stored at different scan rates for (g) NC2 and (h) NC2/NCNTs electrodes, (i) cycling stability of the NC2/NCNTs electrodes at 5000 cycles, respectively.

and surface morphological analyses strongly support the electrochemical study [14,34,53].

After optimizing the specific capacity of the NC1, NC2, NC3, and NC4 electrodes, we systemically developed a strategy to improve the electrochemical performance within the composite of NCNTs electrodes prepared on Ni foam. Fig. 7(a-c) shows the CV curves for the NC2, NCNTs, and NC2/NCNTs composite electrodes with various scan rates. Fig. 7 (b, c) presents the CV measurements for the NCNTs and NC2/NCNTs composites at potential windows of −0.2-0.7 V and −0.1-0.6 V, respectively, with different scan rates of 5-100 mV s^{-1}. As expected, the CV curves for the NC2/NCNTs composite electrode (shown in Fig. 7(c)) showed the highest current density. This composite will be most effective at improving the electrochemical properties of supercapacitors [54]. Fig. 7(d) shows the specific capacity for NC2, NC2/NCNTs, and the NCNTs composite for the various scan rates in the range of 5-100 mV s^{-1}. The specific capacity of the composite electrode was 303 mAh g^{-1} at 5 mV s^{-1}, which was 1.3-fold higher than that of the pristine $NiCo_2O_4$ electrodes (as shown in Fig. S1(d)). This enhancement in electrochemical properties can be ascribed to the positive synergistic effects between $NiCo_2O_4$ and NCNTs nanomaterials. Firstly, highly porous $NiCo_2O_4$ nanoflakes are decorated on the porous 1D hallow nanotubes structures. Secondly, vertically grown $NiCo_2O_4$ nanoflakes and NCNTs nanotubes provided maximum surface area, which is more effective for easy ion transportation. Third and last, interconnected-like network of the nanoflakes and nanotubes hybrid nanostructures indicates, this type of surface provided the higher electrically conductive as well as lower contact resistance, which is useful for faster redox reactions and faster ion exchange process [55,56]. Such hybrid surface morphology provided a maximum specific surface area because 1D hallow nanotubes and 3D nanoflakes are individually activated in the electrochemical reaction [57]. The mechanism of charge storage within the NC2 electrode was scrutinized using the CV curves. The charge-scan rate relation according to the power-law can be written as follows.

$$I = av^b \quad [13]$$

In which, 'a' and 'b' are the adjustable parameters having the definite condition. The b value can be estimated by plotting log(I) against log(ν) depicted in Fig. 7(e). It reveals b = 0.60 for NC2 electrode whereas b = 0.85 for NC2/NCNTs composite electrode denoting contribution of diffusion and capacitive controlled processes. The contribution from the total charge (Q_t) stored by the electrode can be further quantified by assuming that the current response at the fixed potential is the combination of capacitive contribution (Q_s) and diffusion-controlled process (Q_d).

$$Q_t = Q_s + Q_d \quad [14]$$

Considering the semi-infinite linear diffusion, Q_s contribution was calculated by plotting a total charge (Q_t) to the reciprocal square root of the scan rate (Fig. 7(f)) as per the following equation.

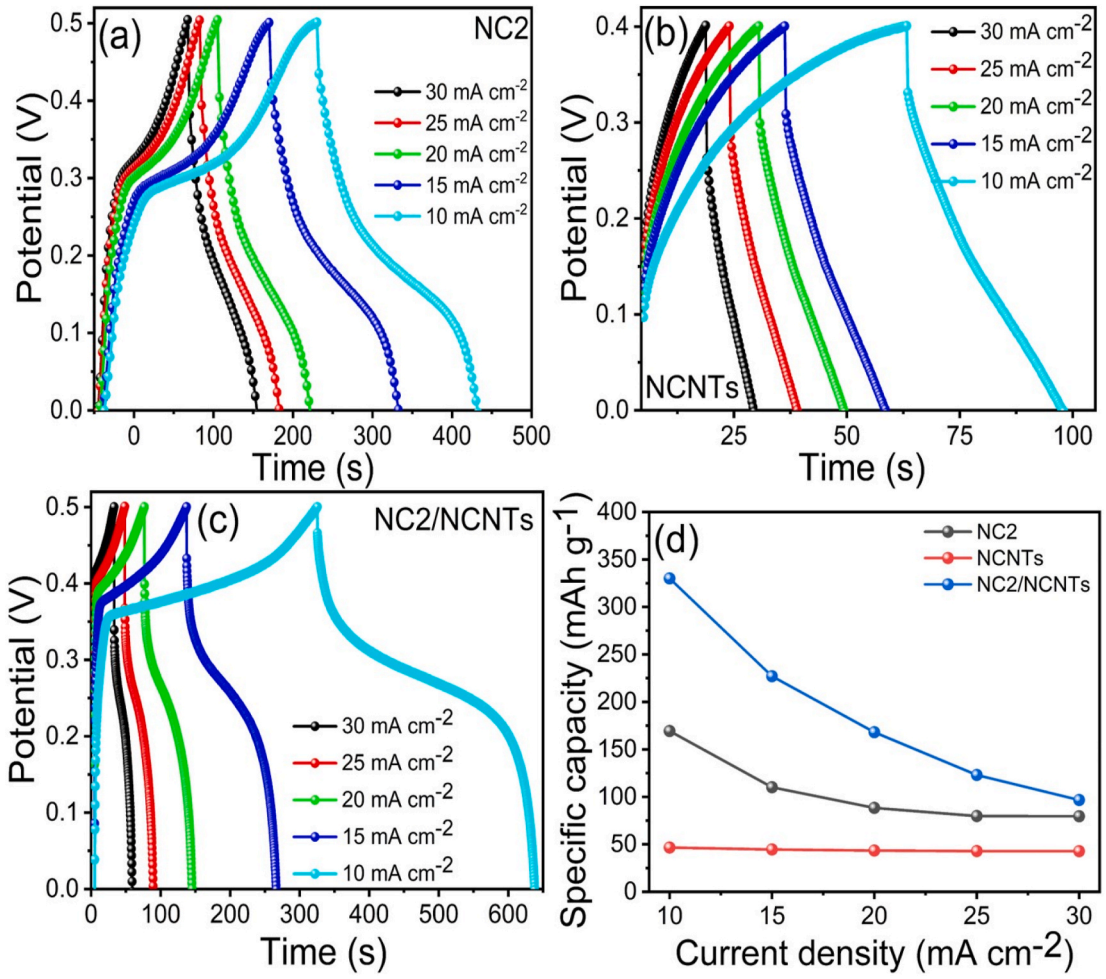

Fig. 8. (a-c) GCD measurements of the NC2, NCNTs, and NC2/NCNTs electrodes at a different current densities, and (d) specific capacity of NC2, NCNTs, and NC2/NCNTs composite with different current densities, respectively.

$$Q_t = Q_d + cv^{-0.5} \quad [15]$$

The total charge contribution that arises from the capacitive-dominated and diffusion-controlled mechanism occurred on the surface of the electrode is depicted separately in Fig. 7(g) and (h) for NC2 and NC2/NCNTs composite electrodes, respectively. It reveals nearly 70 % and 79 % of charges are contributed by the diffusion-controlled processes for NC2 and NC2/NCNTs electrodes at lower scan rate. Fig. 7(i) shows the cycling stability at 100 mV s^{-1} up to 5000 cycles, indicates a good rate of retention (92 %).

After systemic analysis with CV, we performed GCD measurements of pristine NC2, NCNTs, and the NC2/NCNTs composite. Fig. 8(a-c) shows the GCD curves for NC2, NCNTs, and the NC2/NCNTs composite electrode at potential windows of 0-0.5, 0-0.4, and 0-0.5 V with current

Table 1
Comparative study of electrochemical performance $NiCo_2O_4$ materials and other composites.

Ternary compound	Specific capacitance (mAh g^{-1})	Scan rate (mV s^{-1})	Current Density (A g^{-1})	Capability (%)	Potential (V)	Electrolyte M (KOH)	Ref.
$NiCo_2O_4$/NCNTs	330	-	10 mA cm^{-2}	92	0-0.5	3	This work
$NiCo_2O_4$@ $NiMoO_4$	173	-	10 mA cm^{-2}	90	0-0.5	3	7
$NiCo_2O_4$	151	-	1	94	0-0.5	2	20
$NiCo_2O_4$@ $ZnCo_2O_4$	286	-	1	-	−0.2-0.5	2	
$NiCo_2O_4$@ Ni-MOF	209	-	2 mA cm^{-2}	68.2	−0.1-0.5	2	25
$NiCo_2O_4$	140	-	1	93.2	0-0.5	6	27
$NiCo_2O_4$/rGO	112	10		92.28	0-0.6	2	33
$NiCo_2O_4$	125	-	1	94.7	0-0.6	2	41
$NiCo_2O_4$	323	5		94.5	−0.1-0.5	3	50
Co-Al $(OH)_2$	116	-	1	87	0-0.4	6	56
$NiCo_2O_4$@ GQDs	173	-	30	94	0-0.5 V	2	59
$NiCo_2O_4$@ MnO_2	254	-	0.5	87.1	−0.5-0.5	1	64

Table 2
EIS parameters $NiCo_2O_4$ electrodes prepared at various temperature, N-doped CNTs, and composite.

Sample ID	Solution Resistance (R_s)	Charge transferred resistance (R_{ct})
NC1	1.26	0.70
NC2	1.45	0.26
NC3	1.86	2.91
NC4	2.91	14.13
NCNTs	2.45	5.65
NC3/NCNTs	1.95	5.83
NC3/NCNTs//AC Before stability	1.74	0.19
NC3/NCNTs//AC After Stability	6.81	0.26

densities ranging from 10 to 30 mA cm^{-2}. The GCD measurements clearly showed that the nature of all samples was symmetrical with different densities ranging from 10 to 30 mA cm^{-2}, indicating that the samples were stable. The charge/discharge times for NC2, NCNT, and the NC2/NCNT composite were 439, 96, and 646 s, respectively, with the NC2/NCNTs composite having the longest charge/discharge time [54-57]. Compared to the pristine NC2 and NCNTs, the composite electrodes had better electrical properties. Fig. 8(d) shows the calculated specific capacity values for NC2, NCNTs, and the NC2/NCNTs composite electrodes at current densities in the range of 10-30 mA cm^{-2}. The specific capacity values calculated for NC2, NCNTs, and the NC2/NCNTs composite electrodes were 169, 46, and 330 mAh g^{-1} at 10 mA cm^{-2}, respectively. The NC2/NCNTs composite electrode had higher specific capacity values than the pristine NC2 and NCNTs electrodes. The GCD curves clearly showed that the specific capacity decreased as the current density increased, possibly because the redox reaction was completed in a short period [51-55,58]. The higher current density values indicated the NC2/NCNTs composite electrodes had excellent rate capabilities compared to the other electrodes [55,59,60]. More research has been performed on $NiCo_2O_4$ and very few papers have been published on the composites, as shown in Table 1.

EIS measurements were used to determine the correlations and internal charge mechanism for the working electrodes and alkaline 3 M KOH electrolytes. Fig. S2 shows the Nyquist plots for the NC1, NC2, NC3, and NC4 electrodes, respectively. The solution resistance and charge transfer resistance for these samples are listed in Table 2. The NC2 electrode prepared at 323 K had lower solution resistance and charge transfer resistance than the other NC1, NC3, and NC4 samples. The optimized NC2 electrode was used to form a composite with NCNTs to improve the electrical properties [60]. Fig. 9 shows the Nyquist plots for NC2, NCNTs, and the NC2/NCNTs composite electrodes. Compared to the above electrode, the NC2/NCNTs composite had smaller values for charge transfer resistance, suggesting this electrode has high electrical conductivity [61]. Higher electrical conductivity is beneficial for electrochemical performance [62]. The composite of the NC2 and NCNTs electrodes had the lowest charge transfer and solution resistance because the nanostructures of both components are highly mesoporous, similar to nanoflakes/nanotube, and these nanostructures are more suitable for ion diffusion between the electrolytes and electrodes [60-63].

For further practical applications, we constructed pouch-type solid-state hybrid supercapacitor (SSHSc) cells with NC2/NCNTs as a positive electrode denoted as (NC2/NCNTs//AC), AC powder as the negative electrode, and PVA-KOH gel as the conducting electrolyte. The schematic for the construction of the SSHSc cells is shown in Fig. 10(a). Fig. 10(b) shows the optimization of the potential window and the inset shows the specific capacitance of the SSHSc device of NC2/NCNTs//AC determined using CV at a scan rate of 100 mV s^{-1}, respectively. The CV curves indicated that the current sharply increased above 1.2 V; therefore, we employed a potential window of 0-1.2 V for further testing. Fig. 10(c) presents the CV measurements for the SSHSc device of NC2/NCNTs//AC cells at different scan rates in the range of 5-100 mV s^{-1}, and the inset shows the specific capacitance of NC2/NCNTs//AC electrode. The calculated value for the specific capacitance was 170 F g^{-1} at a scan rate of 5 mV s^{-1}, which was better than previously reported (Table 3). The GCD was tested at various current densities in the range of 2-14 mA cm^{-2} as shown in Fig. 10(d) at a potential of 1.2 V. Fig. 10(e) presents the specific capacitance of the SSHSc device of NC2/NCNTs//

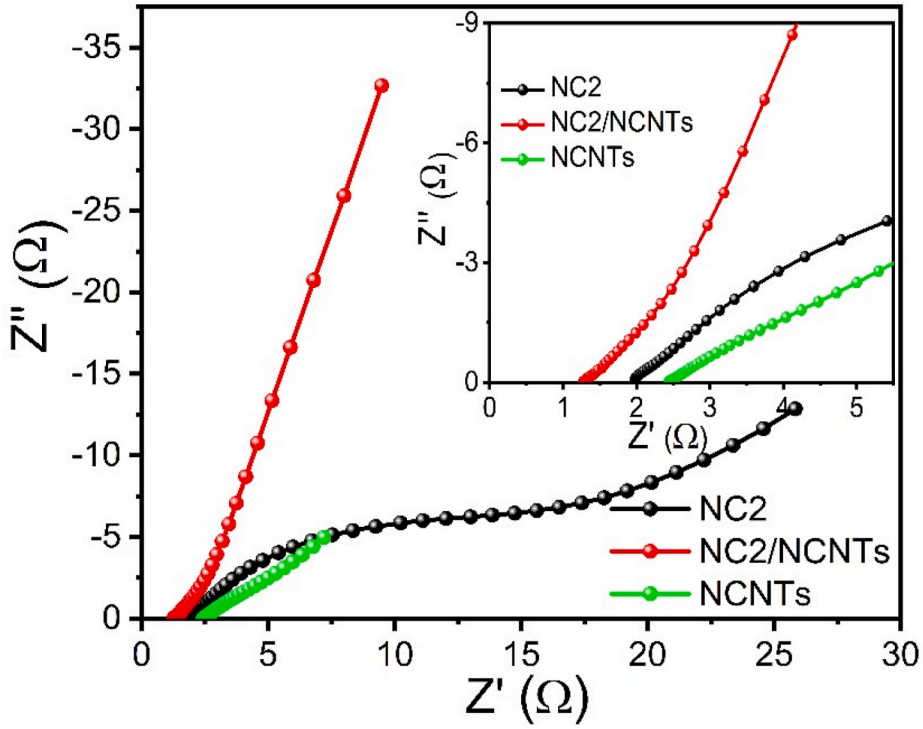

Fig. 9. Nyquist plots of NC2, NCNTs, and NC2/NCNTs composite electrodes, inset shows the high resolution area of the Nyquist plots.

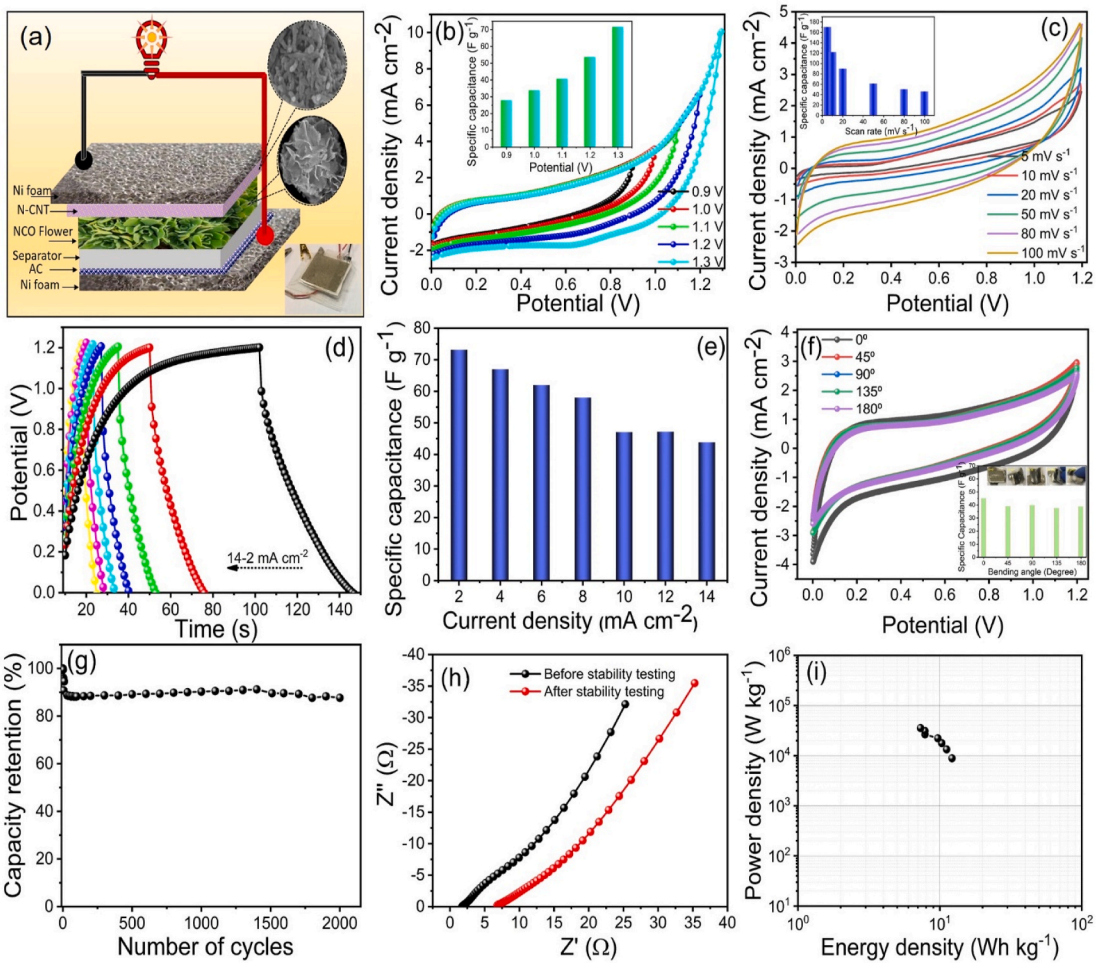

Fig. 10. (a) Schematic assembly of SSHSc device, inset shows the real images of the device, (b) potential window optimization from CV measurements and inset shows the specific capacitance with potential windows, (c) CV curves with different scan rates from 5 to 100 mV s^{-1}, and inset shows the specific capacitance with respect to scan rates, (d) GCD curves with different current densities, (e) specific capacitance with respect with different current densities, (f) bending angle study and inset shows the specific capacitance with real picture of bending device, (g) cycling stability of the SSHSc device, (h) Nyquist plots of before and after cycling stability of the pouch types SSHSc device, (i) Ragone plots of the pouch types SSHSc device..

Table 3
Comparative study of hybrid supercapacitor device of $NiCo_2O_4$ electrodes.

Ternary compound	Specific capacitance (F g^{-1})	Current density (A g^{-1})/ Scan rates	Power density (W kg^{-1})	Energy density (Wh kg^{-1})	Potential (V)	Cycling stability (%)	No of cycles	Ref.
$NICO_2O_4$/ NCNTs@AC	*170*	5 mV s^{-1}	*8.96 kW kg^{-1}*	*12.31*	*1.2*	*84*	*2000*	*This study*
MSBPC/$NiCo_2O_4$	60	1	-	8.47	1.6	85	10,000	34
$NiCo_2O_4$	82.1		875	34.9	1.8	86.4	10,000	41
$NiCo_2O_4$@ HfCNWs/CC	149	1	800	53	1.6	94.8	5000	57
$NiCo_2O_4$@ GQDs	107	1	800	38	1.6	71.8	3000	59
$NiCo_2O_4$/PPy	165	1	365	58.8	1.6	89.2	5000	61

AC electrode with different current densities. The calculated values for the specific capacitance were 73, 67, 62, 58, 47, and 43 F g^{-1} at current densities of 2, 4, 6, 8, 10, and 14 mA cm^{-2}, respectively.

To investigate the mechanical flexibility of the SSHSc devices, we performed bending tests at 0, 45, 90, 135, and 180°, respectively. Fig. 10 (f) show the CV curves with different bending angle and the inset shows the corresponding specific capacitance. No measurable changes were observed after the bending tests, which confirmed the prepared devices had maintained outstanding flexibility and high conductivity [18,64]. Fig. 10(g) shows the stability of the SSHSc device of NC2/NCNTs//AC electrode at 100 mV s^{-1} over 2000 cycles. The stability curves showed that the specific capacitance decreased sharply during the first 100 cycles and remained constant afterward. This indicated that the composite electrode had excellent stability up to 94 %. The stability tests showed that the composite material would be useful in pseudocapacitors. We compared the EIS results before and after 2000 cycles and found that the values for the solution and charge transfer resistance increased slightly after stability testing as shown in Fig. 10(h), indicating that the composite samples did not break after continuous dipping in electrolytes [60,64].

To determine the conductivity of the SSHSc NC2/NCNTs//AC device, we performed EIS before and after cycling testing as shown in Fig. 10(h). The EIS showed lower values for the solution and charge transfer resistance after cycling stability. The EIS measurements showed small changes in the solution and charge transfer resistance, suggesting the devices had higher current and would be more effective for supercapacitor applications [65]. Fig. 10(i) displays the Ragone plot for the SSHSc device of NC2/NCNTs//AC cells. The calculated values for the energy and power density of the SSHSc device of NC2/NCNTs//AC electrode were 12.31 W h kg^{-1}, outstanding power density 8.96 kW kg^{-1}, respectively. The obtained values were comparable with previously reported results (Table 3), indicating the composite of $NiCo_2O_4$ and NCNTs materials is highly suited for pseudocapacitor applications [54,66].

4. Conclusions

We summarized three different chemical methods for the preparation of nanoflowers, nanotubes, and hybrid nanostructures. $NiCo_2O_4$/NCNTs films with uniform deposition over Ni foam were synthesized using a simple and cost-effective chemical method for electrochemical application. $NiCo_2O_4$ materials with various nanostructures were successfully developed at various reaction temperatures. Among these, interconnected hierarchical nanoflowers had the best electrochemical performance because the interconnected plates provided more surface and mesoporous areas and lower resistance. The $NiCo_2O_4$/NCNTs composite had better values for specific capacity (303 mAh g^{-1} at 5 mV s^{-1}) than the pristine $NiCo_2O_4$ electrode (237 mAh g^{-1} at 5 mV s^{-1}). The $NiCo_2O_4$/NCNTs composite had superior electrochemical properties, suggesting that the composite electrode will be more useful in two-electrode devices because of the minimal environmental effect, low cost, and simple synthesis method. Electrochemical analysis of the SSHSc showed that the composite $NiCo_2O_4$/NCNTs flower grown on nanotubes would be a better option for the fabrication of flexible SSHSc devices at the industrial level.

Declaration of competing interest

The authors declare that they have no known competing financial interests or personal relationships that could have appeared to influence the work reported in this paper.

Acknowledgments

Analysis of samples was supported by Dongguk University, Seoul, Korea Research Fund 2020-21, and 2021-2022.

Appendix A. Supplementary data

Supplementary data to this article can be found online at https://doi.org/10.1016/j.ceramint.2021.08.045.

References

[1] D. P Dubal, N. R Chodankar, D.-H. Kim, P. Gomez-Romero, Towards flexible solid-state supercapacitors for smart and wearable electronics, Chem. Soc. Rev. 47 (2018) 2065–2129.
[2] H. Jiang, J. Ma, C. Li, Mesoporous carbon incorporated metal oxide nanomaterials as supercapacitor electrodes, Adv. Mater. 24 (2012) 4197–4202.
[3] Y. Ji, L. Huang, J. Hu, C. Streb, Y.-F. Song, Polyoxometalate-functionalized nanocarbon materials for energy conversion, energy storage and sensor systems, Energy Environ. Sci. 8 (2015) 776–789.
[4] D.P. Dubal, O. Ayyad, V. Ruiz, P. Gómez-Romero, Hybrid energy storage: the merging of battery and supercapacitor chemistries, Chem. Soc. Rev. 44 (2015) 1777–1790.
[5] D.P. Dubal, P. G- Romero, B.R. Sankapal, R. Holze, Nickel cobaltite as an emerging material for supercapacitors: an overview, Nanomater. Energy 11 (2015) 377–399.
[6] M. Saraf, K. Natarajan, S.M. Mobin, Multifunctional porous $NiCo_2O_4$ nanorods: sensitive enzyme less glucose detection and supercapacitor properties with impedance spectroscopic investigations, New J. Chem. 41 (2017) 9299–9313.
[7] Z. Gu, H. Nan, B. Geng, X. Zhang, Three-dimensional $NiCo_2O_4$@$NiMoO_4$ core/shell nanowires for electrochemical energy storage, J. Mater. Chem. 3 (2015) 12069–12075.
[8] N. Kumar, P.K. Sahoo, H.S. Panda, Tuning the electro-chemical properties by selectively substituting transition metals on carbon in Ni/Co oxide-carbon composite electrodes for supercapacitor devices, New J. Chem. 41 (2017) 3562–3573.
[9] Z. Xu, J. Ren, Q. Meng, X. Zhang, C. Du, J. Chen, Facilely hierarchical growth of n-doped carbon-coated $NiCo_2O_4$ nanowire arrays on ni foam for advanced supercapacitor electrodes, ACS Sustain. Chem. Eng. 7 (2019) 12447–12456.
[10] J. Xu, F. Liu, X. Peng, J. Li, Y. Yang, D. Jin, H. Jin, X. Wang, B. Hong, Hydrothermal synthesis of $NiCo_2O_4$/AC composites for supercapacitor with enhanced cycle performance, Chemistry Select 2 (2017) 5189–5195.
[11] D.V. Wagle, H. Zhao, G.A. Baker, Deep eutectic solvents: sustainable media for nanoscale and functional materials, Acc. Chem. Res. 47 (2014) 2299–2308.
[12] Q. Zhang, K.D.O. Vigier, S. Royer, F. Jerome, Deep eutectic solvents: syntheses, properties and applications, Chem. Soc. Rev. 41 (2012) 7108–7146.
[13] S.K. Shinde, S.S. Karade, N.C. Maile, H.M. Yadav, G.S. Ghodake, A.D. Jagadale, D.-Y. Kim, Green synthesis of novel $CuCo_2O_4$ nanocomposite for stable hybrid supercapacitors by deep eutectic solvents, J. Mol. Liq. 334 (2021) 116390, 2021.
[14] Girish S. Gund, Deepak P. Dubal, Supriya B. Jambure, Sujata S. Shinde, Chandrakant D. Lokhande, Temperature influence on morphological progress of Ni $(OH)_2$ thin films and its subsequent effect on electrochemical supercapacitive properties, J. Mater. Chem. 1 (2013) 4793.
[15] M. Sevilla, L. Yu, L. Zhao, C.O. Ania, M.M. Titiricic, Surface modification of CNTs with N-doped carbon: an effective way of enhancing their performance in supercapacitors, ACS Sustain. Chem. Eng. 2 (4) (2014) 1049–1055.
[16] L. Chen, X. Cui, Y. Wang, M. Wang, F. Cui, C. Wei, W. Huang, Z. Hua, L. Zhang, J. Shi, One-step hydrothermal synthesis of nitrogen-doped carbon nanotubes asan efficient electrocatalyst for oxygen reduction reactions, Chem. Asian J. 9 (2014) 2915–2920.
[17] S.K. Shinde, G.S. Ghodake, N.C. Maile, H.M. Yadav, A.D. Jagadale, M.B. Jalak, A. A. Kadam, Sivalingam Ramesh, C. Bathula, D.-Y. Kim, Designing of nanoflakes anchored nanotubes-like $MnCo_2S_4$/halloysite composites for advanced battery like supercapacitor application, Electrochim. Acta 341 (2020) 135973.
[18] A. Mondal, S. Maiti, S. Mahanty, A.B. Pand, Large-scale synthesis of porous $NiCo_2O_4$ and rGO-$NiCo_2O_4$ hollowspheres with superior electrochemical performance as faradaic electrode, J. Mater. Chem. 5 (2017) 16854–16864.
[19] A.J. Christina Mary, C.I. Sathish, P.S.M. Kumar, A. Vinu, A.C. Bose, Fabrication of hybrid supercapacitor device based on $NiCo_2O_4$@$ZnCo_2O_4$ and the biomass-derived N-doped activated carbon with a honeycomb structure, Electrochim. Acta 342 (2020) 136062.
[20] J. Zhang, Q. Mei, Y. Ding, K. Guo, X. Yang, J. Zhao, Ordered mesoporous $NiCo_2O_4$ nanospheres as a novel electrocatalyst platform for 1-Naphthol and 2-Naphthol individual sensing application, ACS Appl. Mater. Interfaces 9 (2017) 29771–29781.
[21] C. Chang, L. Zhang, C.W. Hsu, X.-F. Chuah, S.-Y. Lu, Mixed NiO/$NiCo_2O_4$ nanocrystals grown from the skeleton of a 3D porous nickel network as efficient electrocatalysts for oxygen evolution reactions, ACS Appl. Mater. Interfaces 10 (2018) 417–426.
[22] Y.A. Kumar, H.J. Kim, Preparation and electrochemical performance of $NiCo_2O_4$@ $NiCo_2O_4$ composite nanoplates for high performance supercapacitor applications, New J. Chem. 42 (2018) 19971.
[23] H. Yuan, J. Li, W. Yang, Z. Zhuang, Y. Zhao, L. He, L. Xu, X. Liao, R. Zhu, L. Mai, Oxygen vacancy-determined highly efficient oxygen reduction in $NiCo_2O_4$/Hollow carbon spheres, ACS Appl. Mater. Interfaces 10 (2018) 16410–16417.
[24] H. Cai, X. Li, J. Zhang, D. Zhang, Y. Yang, J. Xiong, Construction of hierarchical $NiCo_2O_4$@Ni-MOF hybrid arrays on carbon cloth as superior battery-type electrodes for flexible solid-state hybrid supercapacitors, ACS Appl. Mater. Interfaces 11 (2019) 37675–37684.
[25] Y. Ha, L. Shi, X. Yan, Z. Chen, Y. Li, W. Xu, R. Wu, Multifunctional electrocatalysis on a porous N-doped $NiCo_2O_4$@C nanonetwork, ACS Appl. Mater. Interfaces 11 (2019) 45546–45553.
[26] Y. Lei, J. Li, Y. Wang, L. Gu, Y. Chang, H. Yuan, D. Xiao, Rapid microwave-assisted green synthesis of 3D hierarchical flower-shaped $NiCo_2O_4$ microsphere for high-performance supercapacitor, ACS Appl. Mater. Interfaces 6 (2014) 1773–1780.
[27] Y. Jia, L. Zhang, G. Gao, H. Chen, B. Wang, J. Zhou, J. Zou, M.T. Soo, M. Hong, X. Yan, G. Qian, J. Zou, A. Du, X. Yao, A heterostructure coupling of exfoliated Ni-Fe hydroxide nanosheet and defective graphene as a bifunctional electrocatalyst for overall water splitting, Adv. Mater. 29 (2017) 1700017.
[28] Z. Chen, R. Wu, M. Liu, Y. Liu, S. Xu, Y. Ha, Y. Guo, X. Yu, D. Sun, F. Fang, Tunable electronic coupling of cobalt sulfide/carbon composites for optimizing oxygen evolution reaction activity, J. Mater. Chem. 6 (2018) 10304–10312.
[29] Z. Yang, C. Zhao, Y. Qu, H. Zhou, F. Zhou, J. Wang, Y. Wu, Y. Li, Trifunctional self-supporting cobalt-embedded carbon nanotube films for ORR, OER, and HER triggered by solid diffusion from bulk metal, Adv. Mater. 31 (2019) 1808043.
[30] G. Zhang, B.Y. Xia, X. Wang, X.W. Lou, Strongly coupled $NiCo_2O_4$-rGO hybrid nanosheets as a methanol-tolerant electrocatalyst for the oxygen reduction reaction, Adv. Mater. 26 (2014) 2408–2412.
[31] S.C. Petitto, E.M. Marsh, G.A. Carson, M.A. Langell, Cobalt oxide surface chemistry: the interaction of CoO (100), Co_3O_4 (110) and Co_3O_4 (111) with oxygen and water, J. Mol. Catal. Chem. 281 (2008) 49–58.
[32] M. Isacfranklin, G. Ravia, R. Yuvakkumar, P. Kumar, Dhayalan Velauthapillai, B. Saravanakumar, M. Thambidurai, C. Dang, Urchin like $NiCo_2O_4$/rGO

nanocomposite for high energy asymmetric storage applications, Ceram. Int. 46 (2020) 16291–16297.
[33] W. Xiong, Y. Gao, X. Wu, X. Hu, D. Lan, Y. Chen, X. Pu, Y. Zeng, J. Su, Z. Zhu, Composite of macroporous carbon with honeycomb-like structure from mollusc shell and $NiCo_2O_4$ nanowires for high-performance supercapacitor, ACS Appl. Mater. Interfaces 6 (2014), 19416−1942.
[34] X. Tong, S. Chen, C. Guo, X. Xia, X.-Y. Guo, Mesoporous $NiCo_2O_4$ nanoplates on three-dimensional graphene foam as an efficient electrocatalyst for the oxygen reduction reaction, ACS Appl. Mater. Interfaces 8 (2016) 28274–28282.
[35] S. Chen, J. Wu, R. Zhou, Y. Chen, Y. Song, L. Wang, Controllable growth of $NiCo_2O_4$ nanoarrays on carbon fiber cloth and its anodic performance for lithium-ion batteries, RSC Adv. 5 (2015) 104433.
[36] S.K. Shinde, M.B. Jalak, G.S. Ghodake, N.C. Maile, V.S. Kumbhar, D.S. Lee, V. J. Fulari, D.-Y. Kim, Chemically synthesized nanoflakes-like $NiCo_2S_4$ electrodes for high-performance supercapacitor application, Appl. Surf. Sci. 466 (2019) 822–829.
[37] S.K. Shinde, D.P. Dubal, G.S. Ghodake, V.J. Fulari, Hierarchical 3D-flower-like CuO nanostructure on copper foil for supercapacitors, RSC Adv. 5 (2015) 4443–4447.
[38] S.K. Shinde, D.P. Dubal, G.S. Ghodake, D.Y. Kim, V.J. Fulari, Nanoflower-like CuO/$Cu(OH)_2$ hybrid thin films: synthesis and electrochemical supercapacitive properties, J. Electroanal. Chem. 732 (2014) 80.
[39] C. Zhang, X. Geng, S. Tang, M. Deng, Y. Du, $NiCo_2O_4$@rGO Hybrid nanostructures on Ni foam as high-performance supercapacitor electrodes, J. Mater. Chem. 5 (2017) 5912–5919.
[40] V. Jose, E. Edison, W.W. Manalastas Jr., S. Sreejith, J.M.V. Nsanzimana, M. Srinivasan, J.-M. Lee, Surface modified hollow ternary $NiCo_2Px$ catalysts for efficient electrochemical water splitting and energy storage, ACS Appl. Mater. Interfaces 11 (2019) 39798–39808.
[41] S. Shinde, H. Dhaygude, D.-Y. Kim, G. Ghodake, P. Bhagwat, P. Dandge, V. Fulari, Improved synthesis of copper oxide nanosheets and its application in development of supercapacitor and antimicrobial agents, J. Ind. Eng. Chem. 36 (2016) 116–120.
[42] S.K. Shinde, D.-Y. Kim, G.S. Ghodake, N.C. Maile, A.A. Kadam, D.S. Lee, M.C. Rath, V.J. Fulari, Morphological enhancement to CuO nanostructures by electron beam irradiation for biocompatibility and electrochemical performance, Ultrason. Sonochem. 40 (2018) 314–322.
[43] H.M. Yadav, G.S. Ghodake, D.-Y. Kim, S. Ramesh, N.C. Maile, D.S. Lee, S.K. Shinde, Nanorods to hexagonal nanosheets of CuO-doped manganese oxide nanostructures for higher electrochemical supercapacitor performance, Colloids Surf., B 184 (2019) 110500.
[44] S.K. Shinde, H.M. Yadav, Sivalingam Ramesh, C. Bathula, Nagesh Maile, G. S. Ghodake, Haridas Dhaygude, D.-Y. Kim, High-performance symmetric supercapacitor; nanoflower-like $NiCo_2O_4$//$NiCo_2O_4$ thin films synthesized by simple and highly stable chemical method, J. Mol. Liq. 299 (2020) 112119.
[45] S.K. Shinde, V.J. Fulari, D.-Y. Kim, N.C. Maile, R.R. Koli, H.D. Dhaygude, G. S. Ghodake, Chemical synthesis of flower-like hybrid $Cu(OH)_2$/CuO electrode: application of polyvinyl alcohol and triton X-100 to enhance supercapacitor performance, Colloids Surf., B 156 (2017) 165–174.
[46] S.K. Shinde, G.S. Ghodake, V.J. Fulari, D.-Y. Kim, High electrochemical performance of nanoflakes like CuO electrode by successive ionic layer adsorption and reaction (SILAR) method, J. Ind. Eng. Chem. 52 (2017) 12–17.
[47] S.K. Shinde, S.M. Mohite, A.A. Kadam, H.M. Yadav, G.S. Ghodake, K.Y. Rajpure, D. S. Lee, D.-Y. Kim, Effect of deposition parameters on spray pyrolysis synthesized CuO nanoparticle thin films for higher supercapacitor performance, J. Electroanal. Chem. 850 (2019) 113433.
[48] S.K. Shinde, M.B. Jalak, G.S. Ghodake, N.C. Maile, H.M. Yadav, A.D. Jagadale, Asif Shahzad, D.S. Lee, A.A. Kadam, V.J. Fulari, D.-Y. Kim, Flower-like $NiCo_2O_4$/$NiCo_2S_4$ electrodes on Ni mesh for higher supercapacitor applications, Ceram. Int. 45 (2019) 17192–17203.
[49] S.K. Shinde, M.B. Jalak, S.Y. Kim, H.M. Yadav, G.S. Ghodake, A.A. Kadam, D.-Y. Kim, Effect of Mn doping on the chemical synthesis of interconnected nanoflakes-like CoS thin films for high performance supercapacitor applications, Ceram. Int. 44 (2018) 23102–23108.
[50] X. Wu, L. Jiang, C. Long, T. Wei, Z. Fan, Dual support system ensuring porous Co-Al hydroxide nanosheets with ultrahigh rate performance and high energy density for supercapacitors, Adv. Funct. Mater. 25 (2015) 1648–1655.
[51] X. Yin, H. Li, Y. Fu, R. Yuan, J. Lu, Hierarchical core-shell structure of $NiCo_2O_4$ nanosheets@HfC nanowires networks for high performance flexible solid-state hybrid supercapacitor, Chem. Eng. J. 392 (2020) 124820.
[52] W. Zuo, C. Xie, P. Xu, Y. Li, J. Liu, A Novel phase-transformation activation process toward Ni-Mn-O nanoprism arrays for 2.4 V ultrahigh-voltage aqueous supercapacitors, Adv. Mater. 29 (2017) 1703463.
[53] J. Luo, J. Wang, S. Liu, W. Wu, T. Jia, Z. Yang, S. Mu, Y. Huang, Graphene quantum dots encapsulated tremella-like $NiCo_2O_4$ for advanced asymmetric supercapacitors, Carbon 146 (2019) 1–8.
[54] Y. Ouyang, H. Ye, X. Xia, X. Jiao, G. Li, S. Mutahir, L. Wang, D. Mandler, W. Lei, Q. Hao, Hierarchical electrodes of $NiCo_2O_4$ nanosheets-anchored sulfur-doped Co_3O_4 nanoneedles with advanced performance for battery-supercapacitor hybrid devices, J. Mater. Chem. 7 (2019) 3228–3237.
[55] D. Kong, W. Ren, C. Cheng, Y. Wang, Z. Huang, H.Y. Yang, Three dimensional $NiCo_2O_4$@Polypyrrole coaxial nanowire arrays on carbon textiles for high-performance flexible asymmetric solid-state supercapacitor, ACS Appl. Mater. Interfaces 7 (2015) 21334–21346.
[56] J. Zhao, Z. Li, X. Yuan, Z. Yang, M. Zhang, A. Meng, Q. Li, A high-energy density asymmetric supercapacitor based on Fe_2O_3 nanoneedle arrays and $NiCo_2O_4$/Ni$(OH)_2$ hybrid nanosheet arrays grown on SiC nanowire networks as free-standing advanced electrodes, Adv. Funct. Mater. 8 (2018) 1702787.
[57] Z.S. Wu, G. Zhou, L.C. Yin, W. Ren, F. Li, H.M. Cheng, Graphene/metal oxide composite electrode materials for energy storage, Nanomater. Energy 1 (2012) 107–131.
[58] Y. Zhang, B. Wang, F. Liu, J. Cheng, X.-W. Zhang, L. Zhang, Full synergistic contribution of electrodeposited three-dimensional $NiCo_2O_4$@MnO_2 nanosheet networks electrode for asymmetric supercapacitors, Nanomater. Energy 27 (2016) 627–637.
[59] N. Wang, B. Sun, P. Zhao, M. Yao, W. Hu, S. Komarneni, Electrodeposition preparation of $NiCo_2O_4$ mesoporous film on ultrafine nickel wire for flexible asymmetric supercapacitors, Chem. Eng. J. 345 (2018) 31–38.
[60] M.-C. Liu, L.-B. Kong, C. Lu, X.-M. Li, Y.-C. Luo, L. Kang, A Sol−Gel process for fabrication of NiO/$NiCo_2O_4$/Co_3O_4 composite with improved electrochemical behavior for electrochemical capacitors, ACS Appl. Mater. Interfaces 4 (2012) 4631–4636.
[61] Y. Ouyang, R. Huang, X. Xia, H. Ye, X. Jiao, L. Wang, W. Lei, Q. Hao, Hierarchical structure electrodes of NiO ultrathin nanosheets anchored to $NiCo_2O_4$ on carbon cloth with excellent cycle stability for asymmetric supercapacitors, Chem. Eng. J. 355 (2019) 416–427.
[62] X. Hu, H. Nan, M. Liu, S. Liu, T. An, H. Tian, Battery-like $MnCo_2O_4$ electrode materials combined with active carbon for hybrid supercapacitors, Electrochim. Acta 306 (2019) 599–609.
[63] J.T. Xu, S.-L. Chou, Q.-F. Gu, M.F.M. Din, H.-K. Liu, S.-X. Dou, Study on vanadium substitution to iron in $Li_2FeP_2O_7$ as cathode material for lithium-ion batteries, Electrochim. Acta 141 (2014) 195–202.
[64] S. Sun, S. Wang, S. Li, Y. Li, Y. Zhang, J. Chen, Z. Zhang, S. Fang, P. Wang, Asymmetric supercapacitors based on a $NiCo_2O_4$/three dimensional graphene composite and three dimensional graphene with high energy density, J. Mater. Chem. 4 (2016) 18646–18653.
[65] J. Zhao, Z. Li, X. Yuan, Z. Yang, M. Zhang, A. Meng, Q. Li, A High energy density asymmetric supercapacitor based on Fe_2O_3 nanoneedle arrays and $NiCo_2O_4$/Ni$(OH)_2$ hybrid nanosheet arrays grown on sic nanowire networks as free-standing advanced electrodes, Adv. Energy Mater. 8 (2018) 1702787.
[66] D. Guo, L. Zhang, X. Song, L. Tan, H. Ma, J. Jiao, D. Zhu, F. Li, $NiCo_2O_4$ nanosheets grown on interconnected honeycomb-like porous biomass carbon for high performance asymmetric supercapacitors, New J. Chem. 42 (2018) 8478–8484.